

Research Article: New Research | Disorders of the Nervous System

## GFAP mutation and astrocyte dysfunction lead to a neurodegenerative profile with impaired synaptic plasticity and cognitive deficits in a rat model of Alexander disease

<https://doi.org/10.1523/ENEURO.0504-24.2025>

Received: 5 November 2024

Revised: 28 January 2025

Accepted: 4 March 2025

Copyright © 2025 Berman et al.

This is an open-access article distributed under the terms of the [Creative Commons Attribution 4.0 International license](#), which permits unrestricted use, distribution and reproduction in any medium provided that the original work is properly attributed.

---

*This Early Release article has been peer reviewed and accepted, but has not been through the composition and copyediting processes. The final version may differ slightly in style or formatting and will contain links to any extended data.*

**Alerts:** Sign up at [www.eneuro.org/alerts](http://www.eneuro.org/alerts) to receive customized email alerts when the fully formatted version of this article is published.

1 GFAP mutation and astrocyte dysfunction lead to a neurodegenerative profile with impaired  
2 synaptic plasticity and cognitive deficits in a rat model of Alexander disease

3

4 Abbreviated title: Neurodegeneration and cognitive deficits in AxD

5 Robert F. Berman,<sup>1,2</sup> Matthew R. Matson,<sup>1</sup> Angelica M. Bachman,<sup>1</sup> Ni-Hsuan Lin,<sup>3</sup> Sierra  
6 Coyne,<sup>4</sup> Alyssa Frelka,<sup>5</sup> Robert A. Pearce,<sup>5</sup> Albee Messing,<sup>4,6</sup> and Tracy L. Hagemann<sup>4</sup>

7 <sup>1</sup>UC Davis M.I.N.D. Institute, University of California Davis, Davis, CA 95816, USA

8 <sup>2</sup>Department of Neurological Surgery, University of California Davis, Sacramento, CA 95816,  
9 USA

10 <sup>3</sup>Institute of Molecular Medicine, College of Life Sciences, National Tsing Hua University,  
11 Hsinchu 30013, Taiwan

12 <sup>4</sup>Waisman Center, University of Wisconsin-Madison, Madison, WI 53705, USA

13 <sup>5</sup>Department of Anesthesiology, University of Wisconsin-Madison, Madison, WI 53705, USA

14 <sup>6</sup>Department of Comparative Biosciences, School of Veterinary Medicine, University of  
15 Wisconsin-Madison, Madison, WI 53706, USA

16 Correspondence should be addressed to Tracy L. Hagemann at [tlhagemann@wisc.edu](mailto:tlhagemann@wisc.edu)

17

18 Number of pages: 40

19 Number of figures: 8 Figures, 5 Extended Data Files

20 Number of tables: 0

21 Number of words      Abstract: 204

22 Introduction: 419

23 Discussion: 1721

24

25 The authors declare no competing financial interests.

26 **Acknowledgements**

27 This work was supported by grants from the NIH NINDS (NS110719 to T.L.H.), NICHD  
28 (HD076892 to A.M., HD105353 and HD090256 core grants to the Waisman Center, and  
29 HD103526 to the Univ. California MIND Institute IDDRCs), NCI (CA014520 core grant to the  
30 University of Wisconsin Carbone Cancer Center), NEI (EY016665 core grant for Vision  
31 Research at the University of Wisconsin-Madison), the Ralph M. Waters Distinguished Chair of  
32 Anesthesiology Fund (to R.A.P.), funds from the National Science and Technology Councils,  
33 Taiwan (NSTC 112-2917-I-007-007 to N.H.L.), and by the Alexander Disease Research Fund.  
34 We thank Lauren Pedersen for her assistance with behavioral experiments at the UC Davis  
35 M.I.N.D. Institute IDDRC.

36 **Abstract**

37 Alexander disease (AxD) is a rare neurological disorder caused by dominant gain-of-function  
38 mutations in the gene for glial acidic fibrillary protein (*GFAP*). Expression of mutant protein  
39 results in astrocyte dysfunction that ultimately leads to developmental delay, failure to thrive,  
40 and intellectual and motor impairment. The disease is typically fatal, and at present there are no  
41 preventative or effective treatments. To gain a better understanding of the link between  
42 astrocyte dysfunction and behavioral deficits in AxD we recently developed a rat model that  
43 recapitulates many of the clinical features of the disease, including failure to thrive, motor  
44 impairment, and white matter deficits. In the present study, we show that both male and female  
45 AxD model rats exhibit a neurodegenerative profile with a progressive neuroinflammatory  
46 response combined with reduced expression of synaptic and mitochondrial proteins. Consistent  
47 with these results AxD rats show reduced hippocampal long-term potentiation and are  
48 cognitively impaired, as demonstrated by poor performance in the Barnes maze and novel  
49 object recognition tests. The AxD rat provides a novel model in which to investigate the impact  
50 of astrocyte pathology on central nervous system function and provides an essential platform for  
51 further development of effective treatments for AxD and potentially other neurodegenerative  
52 diseases with astrocyte pathology.

53 **Significance Statement**

54 Alexander disease (AxD) is a fatal neurodegenerative disorder caused by gain-of-function  
55 *GFAP* mutations. We recently developed a *Gfap*<sup>+R237H</sup> rat model which demonstrates hallmark  
56 astrocyte pathology, myelin deficits, and motor impairment. Here, we show that *Gfap*<sup>+R237H</sup> rats  
57 also exhibit reduced synaptic plasticity and cognitive deficits as additional clinically relevant  
58 phenotypes, further demonstrating its utility as a model. Hippocampal transcriptomic analysis in  
59 young adult animals reveals a neurodegenerative signature with an innate immune response  
60 and loss of synaptic and metabolic gene expression, features that are typically associated with  
61 chronic diseases of aging. These results reveal mechanisms by which astrocyte dysfunction  
62 leads to learning and memory deficits in AxD and perhaps contributes to other diseases such as  
63 Alzheimer's and Parkinson's.

## 64 **Introduction**

65 Alexander disease (AxD) is a progressive and generally fatal disorder of the central nervous  
66 system (CNS), with a range of clinical phenotypes including cognitive and motor impairments  
67 (Messing et al., 2012; Messing, 2019; Hagemann, 2022). In early onset cases, AxD is  
68 associated with prominent white matter deficits, especially in the frontal lobes (van der Knaap et  
69 al., 2001), leading to its original classification as a leukodystrophy, whereas later onset cases  
70 are associated with lesions of the posterior fossa (Prust et al., 2011). In all cases, the hallmark  
71 pathological feature is the presence of Rosenthal fibers, protein aggregates found within the  
72 cytoplasm of astrocytes, particularly in perivascular, subpial, and subependymal locations  
73 (Alexander, 1949). Over 90% of cases of AxD result from heterozygous missense mutations in  
74 the gene encoding the astrocyte intermediate filament, glial fibrillary acidic protein (GFAP)  
75 (Brenner et al., 2001). Since this discovery, AxD has become a model system in which to  
76 explore the consequences of primary astrocyte dysfunction in the CNS (Messing et al., 2012).  
77 Over the past few decades, the role of astrocytes in regulating synapse formation and activity in  
78 both development and disease has become an active area of research (Araque et al., 1999;  
79 Allen and Eroglu, 2017; Blanco-Suarez et al., 2017). Although deficits in the hippocampal  
80 pyramidal layer (CA1) and striatum have been demonstrated in some cases of AxD (Borrett and  
81 Becker, 1985), neuronal loss has not been widely reported (Sosunov et al., 2018).

82 Despite the initial description of AxD as an intellectual disability syndrome (Alexander,  
83 1949), disturbances in cognitive function have received little attention. Generalizations about the  
84 prevalence of the cognitive phenotype in different Alexander disease sub-types are frequently  
85 stated in print, but it is not clear how often and the degree to which patients are cognitively  
86 impaired. Indeed, many questions remain unanswered, including which domains of cognitive  
87 function are affected, whether impairments localize to known sites of pathology, and whether

88 cognitive deficits, once characterized, might be useful as outcome measures in the testing of  
89 experimental treatments.

90 We recently developed a rat model of AxD which demonstrates myelin loss, clinically  
91 relevant motor phenotypes, and increased mortality, more closely recapitulating the human  
92 disease compared to earlier mouse models (Hagemann et al., 2006; Hagemann et al., 2021).  
93 Previous behavior testing in AxD model mice demonstrated deficits in learning and memory  
94 (Hagemann et al., 2013), but these deficits were subtle and strain specific. In this report, we  
95 take advantage of the rat model to investigate whether astrocytes compromised by GFAP  
96 mutation impair synaptic, neuronal, and cognitive function.

97

98

## 99 **Materials and Methods**

### 100 *Rat model of AxD*

101 The *Gfap*<sup>+R237H</sup> rat model of AxD, hereafter referred to as R237H, was generated as previously  
102 described (Hagemann et al., 2021) and maintained as heterozygotes on a Sprague-Dawley  
103 genetic background (Charles River CD IGS rat). All animals were bred at the University of  
104 Wisconsin-Madison. For molecular, histological, and physiological analysis, animals were  
105 housed under specific pathogen free conditions in the AAALAC-accredited Waisman Center  
106 Rodent Models Core. Rats were co-housed as wild type and R237H pairs whenever possible  
107 under a 12-hour light cycle and fed ad libitum. For behavioral phenotyping, rats were bred at the  
108 University of Wisconsin-Madison (UW-Madison) and pregnant dams sent to the University of  
109 California Davis (UC Davis) M.I.N.D. Institute Intellectual and Developmental Disabilities  
110 Research Center (IDDRC). Animals housed at UC Davis were kept under the same conditions  
111 as those in the Waisman Center at UW-Madison (co-housed as wild type and R237H pairs

112 under a 12-hour light cycle and fed ad libitum). All animal studies were approved by the Animal  
113 Care and Use Committees at UC Davis or under the College of Letters and Sciences and Vice  
114 Chancellor Office for Research at UW-Madison.

115

#### 116 *RNA isolation and hippocampal transcriptomics*

117 Male and female littermates of each genotype were sacrificed at 3 or 8 weeks of age by CO<sub>2</sub>  
118 asphyxiation (N = 4 per group, 32 samples total), and hippocampus collected immediately on  
119 ice and frozen (-80°C) before subsequent processing. Hippocampus included Ammon's horn,  
120 the dentate gyrus, and the subiculum. The alveus was used as a dorsal boundary to separate  
121 the hippocampus from subcortical white matter, and parahippocampal regions were removed  
122 from the ventral/lateral boundaries. Excess white matter from the fimbria and fornix were also  
123 removed. RNA was extracted with Trizol reagent per the manufacturer's protocol (Invitrogen,  
124 ThermoFisher Scientific), treated with TURBO DNase (TURBO DNA-free Kit, Ambion,  
125 ThermoFisher Scientific), and RNA integrity determined with an Agilent 4200 TapeStation  
126 System for quality control. Libraries were prepared from 1 µg total RNA with integrity numbers  
127 (RIN) between 8.4 and 9.3 for sequencing with TruSeq Stranded mRNA Sample Preparation kit  
128 (Illumina). Libraries were quantified with PicoGreen reagent (ThermoFisher Scientific) and  
129 assayed with an Agilent TapeStation System to confirm integrity before sequencing with an  
130 Illumina NovaSeq X Plus (2x150bp, 70M reads per sample, 2 lanes). Base calling was  
131 performed using Bcl2fastq (v2.20.0.422), read trimming with Skewer (Jiang et al., 2014), read  
132 alignment with STAR (Dobin et al., 2013), expression estimation with RSEM (Li and Dewey,  
133 2011), and differential expression estimation with EdgeR (Robinson et al., 2010). Pathway  
134 enrichment analysis for differentially expressed genes [false discovery rate (FDR) < 0.01] was  
135 performed with g:Profiler (Raudvere et al., 2019) for Gene Ontology (GO) terms and Kyoto  
136 Encyclopedia of Genes and Genomes (KEGG) pathways (Kanehisa and Goto, 2000), and the



137 full gene list for each comparison over all known rat genes was used as the statistical domain.  
138 Morpheus (<https://software.broadinstitute.org/morpheus>) was used to generate heat maps.  
139 Library preparation, sequencing, and data analysis were performed by the Gene Expression  
140 Center (Research Resource Identifier - RRID:SCR\_017757), the DNA Sequencing Facility  
141 (RRID:SCR\_017759), and the Bioinformatics Core Facility (RRID:SCR\_017799) respectively  
142 within the University of Wisconsin – Madison Biotechnology Center. Results were deposited in  
143 the Gene Expression Omnibus repository under accession number GSE278645.

144

#### 145 *Protein isolation and cytokine analysis*

146 Hippocampal tissues were collected from male and female rats at 8 or 12 weeks of age as  
147 described for RNA extraction. For analysis of cytokines, tissues from 8-week-old rats were  
148 homogenized with a GenoGrinder bead mill in RIPA buffer (Pierce, ThermoFisher Scientific)  
149 with 1 mM Pefabloc SC (Sigma-Aldrich), and Complete Protease Inhibitor Cocktail (Roche,  
150 Sigma-Aldrich) at 150 mg tissue per ml. Samples were centrifuged at 20,000 g for 10 min at  
151 4°C, supernatants collected, and protein quantified using the BCA assay (Pierce, ThermoFisher  
152 Scientific). Homogenates were assayed using the Meso Scale Discovery (MSD)  
153 Proinflammatory Panel 2 (rat) V-PLEX kit to quantify IL1 $\beta$ , IL4, IL5, IL6, IL10, IL13, IFN $\gamma$ , TNF $\alpha$ ,  
154 CXCL1 on a MESO QUICKPLEX SQ 120 multiplex cytokine plate reader within the Small  
155 Molecule Screening Facility at UW-Madison. For analysis of chemokines, tissues from 12-week-  
156 old rats were homogenized with a GenoGrinder bead mill in ProcartaPlex Cell Lysis Buffer  
157 (Invitrogen, ThermoFisher Scientific) with 1 mM Pefabloc SC, and Complete Protease Inhibitor  
158 Cocktail at 200 mg tissue per ml. Samples were centrifuged at 16,000 g for 10 min at 4°C,  
159 supernatants collected, and protein quantified using the BCA assay. Homogenates were  
160 assayed using a ProcartaPlex Rat Chemokine 8-plex Beads panel to quantify CXCL1, CXCL2,  
161 CXCL10, CCL2, CCL3, CCL7, and CCL11 on a Luminex MAGPIX Multiplex Analyzer plate

162 reader within the Vision Research Core at UW-Madison. CXCL1 was below the limit of detection  
163 for the Luminex assay and values from the MSD assay are reported.

164

#### 165 *Protein isolation and western analysis*

166 Hippocampal tissues were collected from male and female rats at 8 weeks of age as described  
167 for RNA extraction above. For analysis of post-synaptic proteins, tissues were homogenized  
168 with a GenoGrinder bead mill in 2% SDS, 50 mM Tris-HCl (pH7.5), 5 mM EDTA, 1 mM Pefabloc  
169 SC (Sigma-Aldrich), and Complete Protease Inhibitor Cocktail (Roche, Sigma-Aldrich) at 50 mg  
170 tissue per ml, and protein quantified using the BCA assay (Pierce, ThermoFisher Scientific).  
171 Protein (5 µg/lane) was separated on 10% TGX Criterion gels (BioRad) and transferred to  
172 Immobilon-IF PVDF membrane. After transfer (30V 15 hrs, Criterion transfer system, 4°C),  
173 membranes were stained with REVERT Total Protein Stain and imaged on an Odyssey imager  
174 (LI-COR Biosciences) for quantification and normalization of proteins of interest. Membranes  
175 were then placed in SEA blocking buffer (Pierce, ThermoFisher Scientific) before proceeding to  
176 incubations with primary antibodies against PSD95 (Cell Signaling 3450) or GluA1 (Cell  
177 Signaling 13185) diluted 1:1000 in TBS with 0.05% Tween20 (TTBS) at 4°C overnight.  
178 Immunoblots were washed 3 times in TTBS, incubated with secondary antibody (1:10,000  
179 IRDye-800CW conjugated goat-anti-rabbit, LI-COR 925-32211) at room temperature for 2  
180 hours, washed again with TTBS followed by PBS, and allowed to dry before analysis with an  
181 Odyssey imager.

182 For vesicular presynaptic proteins and gephyrin, hippocampi were homogenized on ice  
183 in Syn-PER synaptic protein extraction reagent (Pierce, ThermoFisher Scientific) with 1 mM  
184 Pefabloc SC, and Complete Protease Inhibitor Cocktail at 10 mg/ml using a Potter-Elvehjem  
185 tissue homogenizer (900 rpm Teflon pestle in glass tube). Protein from the synaptic fraction (P2

186 per manufacturer's protocol) was quantified with the BCA assay and 1  $\mu$ g loaded (without  
187 heating) on 10% separating gels and transferred to nitrocellulose at 100 V for 70 min.  
188 Membranes were blocked in TTBS with 5% BSA before proceeding to protein staining (as  
189 above) and incubating with primary antibodies against SV2A (Cell Signaling 66724), VGluT1  
190 (Cell Signaling 47181), VGAT (Synaptic Systems 131 004), or gephyrin (Proteintech 12681-1-  
191 AP) diluted 1:1000 in TTBS overnight at 4°C. Immunoblots were washed 3 times in TTBS,  
192 incubated with peroxidase conjugated goat anti-mouse, rabbit, or guinea-pig secondary  
193 antibodies (Jackson ImmunoResearch Laboratories, 115-035-003, 111-035-003, 106-035-003,  
194 diluted 1:5000) at room temperature for 2 hours, washed again with TTBS before developing  
195 with Western Lightning Plus chemiluminescent substrate (Perkin Elmer) and imaging with an  
196 Azure 500 system.

197 For mitochondrial proteins, hippocampi were homogenized on ice in RIPA buffer (Pierce,  
198 ThermoFisher Scientific) with 1 mM Pefabloc SC, and Complete Protease Inhibitor Cocktail at  
199 10 mg/ml using a Potter-Elvehjem tissue homogenizer (900 rpm). Homogenates were  
200 centrifuged at 12,000 g, protein from the supernatant quantified with the BCA assay, and 8  $\mu$ g  
201 loaded (without heating) on a 12% separating gel and transferred to PVDF in Bjerrum &  
202 Schafer-Nielsen transfer buffer at 100 V for 70 min. Immunolabeling was performed using the  
203 Total OXPHOS Rodent Western Blot Antibody Cocktail (Abcam ab110413) as described for  
204 synaptic proteins.

#### 205 206 *Immunolabeling and stereology*

207 Animals were deeply anesthetized with isoflurane and transcardially perfused with saline  
208 followed by 4% paraformaldehyde. Brains were removed and post-fixed in paraformaldehyde  
209 before cryoprotecting in 30% sucrose and collecting 40  $\mu$ m coronal sections on a sliding

210 microtome. For stereology, every 6<sup>th</sup> section (240  $\mu\text{m}$  interval) starting at the rostral extent of the  
211 hippocampus (approximately -1.4 mm from bregma) was immunolabeled for NeuN to count  
212 neuronal nuclei in the pyramidal layers and the granule cell layer of the dentate gyrus.  
213 Pyramidal cell nuclei in CA1 and CA3 and dentate granule cell nuclei were outlined separately  
214 using Stereo Investigator (MBF Bioscience) for both hippocampi for a total of 6 contours per  
215 section when all regions were present. Cell counting was performed in both hemispheres on  
216 sections anterior to the posterior commissure (approximately -4.5 bregma). For rats at 8 weeks  
217 of age, the sampling grid was 180 x 180  $\mu\text{m}$ , the counting frame was 20 x 20  $\mu\text{m}$ , and the  
218 disector height was 25  $\mu\text{m}$ . For rats at 3 weeks, the sampling grid was 150 x 150  $\mu\text{m}$ , the  
219 counting frame was 20 x 20  $\mu\text{m}$ , and the disector height was 20  $\mu\text{m}$ . Even numbers of males  
220 and females were analyzed in both age groups (N=3) and data combined for the final analysis  
221 after confirming there was no significant effect of sex. The Gundersen coefficient was less than  
222 0.1 (m=1) for all samples, and the total cell population was estimated for the dorsal  
223 hippocampus using the mean section thickness.

224

### 225 *Hippocampal long-term potentiation*

226 *Slice preparation:* Coronal hippocampal slices (400  $\mu\text{m}$ ) were prepared from 16-week-old rats.  
227 The rats were deeply anesthetized using isoflurane and decapitated. The brain was removed  
228 from the skull within 60 seconds of decapitation and immediately placed in a slice preparation  
229 solution containing 124 mM NaCl, 1.25 mM  $\text{NaH}_2\text{PO}_4$ , 3 mM KCl, 25 mM  $\text{NaHCO}_3$ , 10 mM  
230 glucose, 1 mM sodium ascorbate, 3 mM kynurenic acid, 3.6 mM  $\text{MgSO}_4$  and 0.8 mM  $\text{CaCl}_2$  and  
231 saturated with carbogen (95%  $\text{O}_2$ /5%  $\text{CO}_2$ ). Brain slices were cut with a vibratome (Model 7000  
232 smz2, Campden Instruments, Loughborough, UK) and transferred into a submerged incubation  
233 chamber containing slice recovery solution of 124 mM NaCl, 3 mM KCl, 1.25 mM  $\text{NaH}_2\text{PO}_4$ , 25  
234 mM  $\text{NaHCO}_3$ , 15 mM glucose, 0.8 mM sodium ascorbate, 1.3 mM  $\text{MgSO}_4$ , and 2.5 mM  $\text{CaCl}_2$ .

235 Slices were recovered at 33°C for 30 minutes followed by a room temperature recovery for  
236 60 minutes. Both the preparation and recovery solutions were buffered to pH 7.3 with an  
237 osmolality between 294–297 osmol/kgH<sub>2</sub>O.

238 *Long-Term Potentiation (LTP)*: Recordings were taken from coronal slices in a  
239 submersion recording chamber perfused with the carbogenated recovery solution at 3.0 mL/min  
240 at 30°C using fire-polished borosilicate glass recording pipettes filled with 1 M NaCl (3–5 MΩ)  
241 and evoked responses were generated using Pt/Ir concentric bipolar stimulating electrodes.  
242 WinLTP software (v2.3, Bristol University) was used for stimulation and recording. LTP was  
243 induced using three theta burst trains consisting of 40 stimuli grouped into 10 bursts of 4 stimuli  
244 each at 100 Hz with burst delivered at 5 Hz. Potentiation was defined as the mean field  
245 excitatory postsynaptic potential (fEPSP) slope during the last 10 minutes of the 60-minute LTP  
246 recording compared to the average fEPSP slope during the 10-minute period preceding the  
247 theta burst stimulus.

#### 248 *Novel object recognition*

249 A total of 6 litters were used to generate 2 cohorts of R237H and wild type littermates (N=24  
250 with 12 males and 12 females per genotype) for the novel object recognition (NOR) test.  
251 Animals were tested at 16 weeks of age. Testing took place in a black Plexiglas arena (60 x 60  
252 x 50 cm) over two consecutive days. On day 1, rats were placed in an empty arena for 30 min to  
253 habituate them to the apparatus, and then returned to their home cage. On day 2, the  
254 familiarization phase, they were returned to the empty arena and allowed another 30 min of  
255 habituation. Two identical objects were then placed into the arena with the animals, and they  
256 were allowed 10 minutes to freely explore the two objects. Following exploration of the now  
257 familiar objects, rats were removed from the arena and isolated in Plexiglas holding cages for at  
258 least 60 minutes. One of the two objects was then replaced with a novel object. Rats were  
259 returned to the testing arena and allowed 5 minutes to freely explore the familiar and novel  
260 objects. Time spent exploring the objects was determined and used to generate a discrimination

261 index (DI, time exploring novel object/total time exploring both novel and familiar objects) as a  
262 measure of novel object recognition and memory for previously seen objects (Ennaceur and  
263 Delacour, 1988; Winters et al., 2008; Kinnavane et al., 2015). A glass jar and plastic cone were  
264 used as the stimulus objects. Right/left object position and designation of jar/cone as  
265 novel/familiar objects were counter-balanced across experimental groups. All trials were  
266 tracked using EthoVision software (EthoVision v.13.0, Noldus Information Technology,  
267 Netherlands) and time with the familiar and novel object was hand-scored by the investigator.  
268

### 269 *Barnes maze*

270 A total of 13 litters were used to generate 2 cohorts of R237H (N=24; 11 males, 13 females) and  
271 wild type (N=30; 14 males, 16 females) littermates for the Barnes maze test (separate cohorts  
272 from those tested for NOR). Animals were tested at 16 weeks of age. The Barnes maze  
273 consists of a circular black Plexiglas test arena (170 cm in diameter) with 20 circular holes (12  
274 cm in diameter) around the perimeter. One hole is designated as the escape hole and has a  
275 dark goal box underneath which the rat can enter. Rats were tested for a total of 6 days, with  
276 one habituation day and 5 training days. The maze was surrounded by black curtains and visual  
277 cues (e.g., white square, circle, triangle, and "N" shape) were attached to the curtain and  
278 present throughout training. On habituation day, the rats were placed on the arena for 10  
279 minutes with ambient light (30 lux), with no curtain cues or goal box present. They were then  
280 returned to their home cage. The following day, rats were placed under a black Plexiglas box  
281 (approximately 20 x 20 x 15 cm) in the center of the arena for 60 seconds. Bright lights of  
282 approximately 1,000 lux and approximately 60 dB of white noise were then turned on. After 60  
283 seconds, the rat was released from the box and was given 90 seconds to find the escape hole.  
284 If the rat did not find the escape hole, the investigator led the rat to the hole. In both cases,  
285 lights and sound were turned off when the rat entered the escape hole. The rat then remained in  
286 the escape hole for 15 seconds before starting the next trial. Each rat had 4 trials per day over

287 the 5-day testing period. During each trial, the investigator recorded the latency to reach the  
288 escape hole (whether or not they escaped), total distance traveled, and search strategy used on  
289 the maze (random, serial, or direct) as described previously (Fedor et al., 2010; Pitts, 2018).  
290 Briefly, spatial strategies included a direct (the rat goes directly to the escape hole with no  
291 incorrect holes chosen) or serial search around the perimeter of the maze in either the  
292 clockwise or counterclockwise direction visiting 2 or more holes. All other patterns of movement  
293 on the maze were classified as random. Latency to locate the escape hole and spatial search  
294 strategy were analyzed.

295

#### 296 *Statistical analyses*

297 Data resulting from molecular, histological, and physiological analyses were analyzed using  
298 GraphPad Prism. For data sets with a single variable, an unpaired 2-tailed *t*-test was used to  
299 determine significance. For data sets with 2 variables, a 2-way ANOVA was used to determine  
300 significance. All data in graphs represent means  $\pm$  standard deviation.

301 Behavioral data were analyzed using SPSS statistical package (IBM SPSS Statistics,  
302 Version 28.0.0.0.). For the NOR test, time spent exploring the familiar and novel objects were  
303 analyzed by a two-way repeated measures ANOVA. A discrimination index (DI) calculated as  
304 the ratio of time spent exploring the novel object divided by the total time spent exploring the  
305 novel and familiar objects (i.e., novel/novel + familiar). Using this index, a lack of preference for  
306 novel vs familiar objects yields a DI of 0.5. A one sample *t*-test was used to determine whether  
307 the DI differed significantly from 0.5 and was used as an index of the strength of recognition  
308 memory (Brown and Aggleton, 2001). The DI corresponds to  $d'$ , one of the primary measures of  
309 recognition memory in humans (Sivakumaran et al., 2018). Latency to find the escape hole in  
310 the Barnes maze was analyzed by a mixed effects model with Šídák's multiple comparisons

311 post-test. Search strategy (direct, serial, and random, as described in Barnes maze methods  
312 above) used to locate the escape hole was analyzed by Chi square.

313 Data were examined for missing values and outliers. Outliers were identified from z-  
314 transformed data as those exceeding  $\pm 3.29$ . Missing data and outliers were replaced by  
315 multiple imputation (SPSS). Levene's test for homogeneity of variance was carried out and  
316 variables violating assumptions of homogeneity were analyzed via the Mann-Whitney U non-  
317 parametric statistic. All tests were 2-tailed with the minimum probability to establish statistical  
318 significance set at  $p < 0.05$ . All data in graphs represent means  $\pm$  standard error of the mean ( $\bar{X} \pm$   
319 SE). The minimum probability for statistical significance was set at  $p < 0.05$ . Experimenters were  
320 blinded to genotype throughout behavioral testing, although the smaller size of R237H versus  
321 WT rats was readily apparent from approximately 5 weeks of age and this difference continued  
322 through the experiments (see Figure 1F, (Hagemann et al., 2021)).

323

324

## 325 **Results**

### 326 **Neurodegenerative profile of hippocampal transcripts in R237H rat model of AxD**

327 The R237H rat model of AxD exhibits extensive GFAP accumulation and aggregation  
328 throughout the CNS, with a particularly high pathological burden in hippocampus (Hagemann et  
329 al., 2021). Given the role of hippocampus in learning and memory, we wanted to understand the  
330 impact of reactive glia and astrocyte dysfunction on neurons and cognitive function and began  
331 with bulk RNA sequencing for differential gene expression analysis. To distinguish initiating  
332 events from chronic disease, we collected hippocampus at 3 weeks of age (P21), when CNS  
333 pathology is apparent but R237H rats are otherwise presymptomatic, and at 8 weeks of age  
334 (P56), when pathology is significantly worse and the rats are severely affected with motor  
335 impairment and increased mortality. Both male and female R237H rats were analyzed with wild



336 type littermate controls, and gene expression comparisons were made between genotypes  
337 within age groups. In both age groups, elevated transcripts in the R237H rat hippocampus (FDR  
338 < 0.01) were dominated by immune related genes which demonstrated the largest fold changes.  
339 Those that were decreased encoded proteins related to synaptic and metabolic function (Fig.  
340 1A, P56 males shown; Extended Data Fig. 1-1, 1-2, 1-3, and 1-4). Given the large number of  
341 genes that were affected (Fig. 1B), those that were upregulated were analyzed for pathway  
342 enrichment separately from genes that were downregulated (2747 increased, 1907 decreased,  
343 FDR < 0.01 in P56 male R237H rats). Enrichment results for gene ontology (GO) terms were  
344 filtered using a two-stage algorithm within g:Profiler to group significant terms into sub-  
345 ontologies and identify functional drivers within these contexts (Raudvere et al., 2019). At 8  
346 weeks of age when disease is most severe, molecular functions of genes with increased  
347 expression were related to cytokine and immune receptor binding and activity, integrin binding,  
348 and downstream effects such as protein kinase binding (Fig 1C, males shown; Extended Data  
349 Fig. 1-1 and 1-2). Enriched biological processes again included immune system components  
350 and integrin mediated signaling pathways as related drivers. Actions involved in reactive gliosis,  
351 including cytoskeletal and extracellular matrix reorganization (e.g., actin filament and  
352 supramolecular fiber organization) and pathways related to cell cycle, were also highlighted as  
353 driving processes. Enriched cellular components included lytic vacuoles (lysosomes), vesicles  
354 (including endosomes) and cell adhesion terms such as focal adhesions, integrins, and  
355 associated signaling molecules (Fig 1C; Extended Data Fig. 1-1 and 1-2).

356 KEGG pathway enrichment analysis demonstrated activation of NFkB and JAK-STAT  
357 signaling (Fig 1C), consistent with our previous report showing both NFkB and STAT3 are  
358 activated in R237H rat hippocampus (Hagemann et al., 2021). Transcripts related to cellular  
359 senescence and p53 signaling, including *Cdnk1a* (p21WAF), cyclins and checkpoint kinases,  
360 GADD45 genes, and Tp53 itself, were also significantly enriched, corroborating our recent work  
361 showing astrocyte senescence in the rat as well as other models of AxD (Wang et al., 2022).

362 Pathways associated with an innate immune response were highly enriched, and a response to  
363 danger/pathogen associated molecular patterns (DAMPs and PAMPs) through NOD-like, Toll-  
364 like, and C-type lectin receptor signaling, cytosolic DNA-sensing, and RIG-1-like receptor  
365 signaling could further contribute to astrocyte senescence and the associated secretory  
366 phenotype (SASP) (Li and Chen, 2018). It is noteworthy that lymphocyte-related pathways are  
367 enriched, and although these pathways overlap with other immune-related categories, T-cell  
368 infiltration has been documented in AxD (Olabarria et al., 2015; Boyd et al., 2021). Comparisons  
369 between age groups showed that a majority of elevated transcripts were increased at both 3-  
370 and 8-weeks, with enrichment for most of the same immune related pathways in each group  
371 (Fig. 1D,E). A heat map of significantly increased innate immune related transcripts shows a  
372 subset of genes with comparable increases at both presymptomatic (P21) and severe stages  
373 (P56) while other transcripts demonstrate a progressive increase as the animals age (Fig. 1D;  
374 Extended Data Fig. 1-1, 1-2, 1-3, and 1-4). Many of the increased transcripts with an FDR <  
375 0.01 at P21 and not at P56 (425 transcripts, Fig. 1B) were elevated at P56 when an FDR < 0.05  
376 was considered (97/425). Of the 425 unique transcripts elevated at P21, 101 were down  
377 regulated in R237H rats at P56 compared to R237H rats at P21; however, there were no  
378 common pathways associated with these genes.

379 Transcripts which were decreased in the R237H rat consisted of genes related to  
380 synapses and metabolism and depicted a neurodegenerative profile (Fig. 1A). GO term  
381 enrichment analysis for molecular function at 8 weeks of age showed decreased expression of  
382 inorganic cation transmembrane transporters (proton, metal ion, and potassium transporters),  
383 channel regulators, and proteins involved in glutamate receptor binding. Synaptic signaling and  
384 synaptic organization drove biological processes, with all terms relating to synaptic function  
385 including G protein-coupled receptor signaling, monoatomic ion transport (potassium, calcium,  
386 metal ion transport), and aerobic respiration (mitochondrial function). Enriched cellular  
387 components also consisted of synapse related terms which included mitochondrial membranes

388 and the respiratory chain complex. Many of these changes were not yet apparent at 3 weeks of  
389 age in asymptomatic rats (Fig. 1D,E; Extended Data Fig. 1-3, 1-4). Enriched GO terms in rats at  
390 P21 included monoatomic ion transport and nervous system development as drivers of  
391 molecular function and biological process respectively, but only cellular component terms  
392 showed a significant enrichment of synapse related compartments (Fig. 1D,E; Extended Data  
393 Fig. 1-3, 1-4).

394 KEGG pathway enrichment analysis for transcripts that were decreased at 8 weeks of  
395 age in R237H rat hippocampus again highlighted a neurodegenerative profile and included  
396 “pathways of neurodegeneration – multiple diseases”, as well as Alzheimer, Parkinson, and  
397 Huntington disease, and amyotrophic lateral sclerosis (ALS). Multiple synaptic profiles,  
398 including those for glutamatergic, GABAergic, cholinergic, dopaminergic, and serotonergic  
399 synapses, showed decreased expression, as predicted by GO term analysis. Transcripts related  
400 to oxidative phosphorylation and mitochondrial function were highly enriched among  
401 downregulated genes, and genes related to calcium and cyclic AMP signaling also showed  
402 decreased expression (Fig. 1C). At 3 weeks of age, pathways of neurodegeneration were not  
403 significantly enriched in R237H rats. Comparisons of expression changes for synapse related  
404 genes (GO:0045202) between age groups demonstrated expected developmental changes  
405 (within both genotypes) but a general trend for decreases in AxD model rats at both  
406 presymptomatic and severe disease stages (Fig. 1D,E). A higher number of genes related to  
407 mitochondrial function were downregulated at 8 weeks compared to 3 weeks, accounting for the  
408 shift to a neurodegenerative profile at the later age (Fig. 1D,E). Genes encoded by  
409 mitochondrial DNA (mtDNA) were not downregulated at P21, but transcripts from all 13 protein  
410 encoding genes were decreased at P56 as well as many nuclear genes related to oxidative  
411 phosphorylation and respiration, suggesting an overall reduction of mitochondrial function at this  
412 severe stage of disease (Fig. 1D).

413

#### 414 **Neuroinflammatory response to GFAP mutation in AxD model rats**

415 We have previously demonstrated activation of NF $\kappa$ B and STAT3 in R237H rat hippocampus,  
416 and specifically nuclear localization of phosphorylated STAT3 (Tyr705) in astrocytes  
417 (Hagemann et al., 2021). Here, to determine whether elevation of immune related transcripts  
418 translated into a neuroinflammatory microenvironment, we quantified cytokines and small  
419 chemokines in adult rat hippocampus by ELISA (Fig. 2A). In agreement with STAT3 activation  
420 and our previous report showing a senescence phenotype in AxD astrocytes (Wang et al.,  
421 2022), IL6 was markedly elevated (24-fold,  $p < 0.0001$ ), and TNF $\alpha$  was also significantly  
422 increased (2-fold,  $p < 0.0001$ ), similar to their transcription profile (Fig. 2B). Although IL1 $\beta$   
423 transcript is elevated, protein was slightly decreased, and many of the other interleukins  
424 analyzed were near the lower limits of detection and only marginally elevated, including anti-  
425 inflammatory cytokines IL10 and IL4. It is possible that the assay used may not detect pro-IL1 $\beta$   
426 or oxidized/reduced forms (per the manufacturer) or that heterogeneous nuclear  
427 ribonucleoproteins may affect translation (Sirenko et al., 2002; Zhao et al., 2012). Many small  
428 chemokines were highly elevated, including CXCL1 and CCL2, suggesting potential  
429 chemotactic effects on peripheral immune cells. CXCL10, an IFN $\gamma$  inducible chemokine, is also  
430 markedly elevated, although IFN $\gamma$  is only marginally increased.

431

#### 432 **Regional differences in hippocampal neuron numbers**

433 The decrease in synapse related gene expression observed in the R237H rat hippocampus  
434 (Fig. 1C) could reflect neuronal loss, and we have previously reported that granule cells in the  
435 hippocampal dentate gyrus are reduced in number (Hagemann et al., 2021). To analyze both  
436 the dentate gyrus and pyramidal cell layers, we counted pyramidal cells in CA1 and CA3 and  
437 granule cells in the dentate gyrus of the dorsal hippocampus using stereological methods at 3  
438 and 8 weeks of age. At 3 weeks of age, there were no differences in the regions analyzed;  
439 however, a reduction in granule cell numbers was confirmed in the dentate gyrus at 8 weeks of

440 age (Fig. 3). This is of particular interest in view of the involvement of the dentate gyrus in the  
441 formation of precise memories for locations of objects (Lee and Jung, 2017). No change in  
442 pyramidal cell numbers were detected in CA1 or CA3 at 8 weeks (Fig. 3).

443

#### 444 **Neurodegenerative changes in synaptic and mitochondrial proteins in R237H rat** 445 **hippocampus**

446 To further assess neuronal pathology and potentially synapse function, we quantified  
447 expression of synapse related proteins in hippocampus from R237H rats at 8 weeks of age. An  
448 initial assessment by western analysis showed decreases in both pre- and post-synaptic  
449 proteins including SV2A (synaptic vesicle glycoprotein 2A) and PSD95 (postsynaptic density  
450 protein 95) respectively (Fig. 4A,B). More specific analysis of excitatory synaptic markers  
451 VGluT1 (vesicular glutamate transporter 1) and GluA1 (AMPA glutamate receptor subunit A1)  
452 also demonstrated decreases at the protein level (Fig. 4C,D). Inhibitory pre- and post-synaptic  
453 markers VGAT (vesicular GABA transporter) and gephyrin were also reduced (Fig. 4E,F). In  
454 addition, we analyzed a panel of mitochondrial proteins related to oxidative phosphorylation  
455 (Fig. 5) from complex I through V (NDUFB8, SDHB, UQCRC2, MT-CO1, ATP5A). All but  
456 complex V (ATP5A) showed a decrease in R237H rat hippocampus at 8 weeks of age, including  
457 the mitochondrially encoded cytochrome C oxidase I (complex III and IV).

458

#### 459 **Deficits in hippocampal long-term potentiation in R237H rats**

460 To determine whether differences in expression of synaptic proteins translated into physiological  
461 deficits, we analyzed R237H rat hippocampus for long-term potentiation (LTP) in Schaffer  
462 collateral-CA1 synapses. To match the age at which we planned to test cognitive function, LTP  
463 was measured at 16 weeks, when R237H rats show improved motor performance and are past  
464 the critical survival period between 6-12 weeks of age when 15% of the animals die. Acute

465 coronal slices including the dorsal hippocampus were collected from both male and female rats  
466 of each genotype and subjected to a theta-burst stimulation (TBS) paradigm with three trains of  
467 10 bursts (4x100Hz). The field excitatory postsynaptic potential (fEPSP) was measured for 10  
468 minutes before and one hour after TBS. Potentiation for each slice was defined as the mean  
469 fEPSP slope during the final 10 minutes compared to baseline (Fig. 6A). There was significantly  
470 less potentiation ( $p = 0.0008$ , *t*-test) for R237H rats versus wild type rats, confirming impaired  
471 synaptic plasticity at this age in the model (Fig. 6B).

472

### 473 **Deficits in novel object recognition in R237H rats**

474 The novel object recognition (NOR) task was used as an initial test to evaluate recognition  
475 memory in the R237H rat. This test is based on the tendency of rats to spend more time  
476 exploring novel objects than exploring familiar objects (Ennaceur and Delacour, 1988). Current  
477 evidence supports a critical role for the perirhinal cortex and its projections to the hippocampus,  
478 including the dentate gyrus, in object memory encoding, consolidation, and retrieval (Brown and  
479 Aggleton, 2001; Winters et al., 2008; Kinnavane et al., 2015). R237H rats and littermate controls  
480 were tested at 16 weeks of age. Wild type rats showed longer exploration of the novel object  
481 compared to the familiar object with a significant effect of genotype (two-way RM ANOVA,  $p =$   
482  $0.0001$ ), while R237H rats did not show a preference (Fig. 7A, data from one female R237H rat  
483 was excluded from analysis due to a lack of exploratory activity during the testing phase). A  
484 discrimination index (DI) representing the time exploring the novel object as a fraction of the  
485 total time exploring both objects was calculated as an additional measure of NOR performance.  
486 DIs for recognition memory performance in male ( $*p = 0.018$ ) and female wild type ( $**p = 0.006$ )  
487 rats were significantly greater than 0.5 (i.e., chance) indicating memory for previously presented  
488 objects (Fig. 7B). In contrast, DIs were not significantly above chance for either male or female  
489 R237H rats.

490

## 491 **Impaired Barnes maze performance in R237H rats**

492 The Barnes maze is a behavioral test of spatial memory (Barnes, 1979). It shares similarities  
493 with the Morris water maze (Morris, 1984) in that it requires an animal to use distal  
494 environmental cues to locate a fixed escape location and has the advantage of not requiring  
495 stress associated with swimming. The goal of this task is for the rats to learn to seek shelter  
496 from bright lights by finding a dark escape hole. Male and female R237H rats and littermate  
497 controls were tested with 4 trials per day over 5 consecutive days at 16 weeks of age, and data  
498 were analyzed separately for each day as well as the average daily score across the four daily  
499 trials using a day-by-genotype-by-sex repeated measures ANOVA. Data for trial 1 on each test  
500 day was used to assess spatial reference in the Barnes maze and proved to be the most  
501 reliable as rats tended to perform poorly over repeated trials each day once they had located  
502 the escape hole in trial 1. Figure 8A shows the average latency (seconds) to find the escape  
503 hole in trial 1 on each of the 5 testing days. As expected, there was a significant overall  
504 decrease in latency to find the escape hole ( $F_{4,188} = 9.80, p < 0.001$ ) across test days. There was  
505 also a significant difference between genotypes ( $F_{1,47} = 4.74, p < 0.05$ ). Sex differences and  
506 interactions were not statistically significant. Comparisons of daily escape latencies between  
507 wild type and R237H rats showed that wild type rats had shorter escape latencies on test day 5  
508 compared to R237H rats ( $F_{1,52} = 4.22, p < 0.05$ ). Escape latencies did not differ on test days 1-4.  
509 The three nominal search strategies used by the rats (random, serial, or direct) were also  
510 analyzed for Trial 1 on each test day, as well as the average percent use of each strategy over  
511 the four trials on each test day. As shown in Figure 8B, rats begin the task by using mainly a  
512 random search strategy but shift to serial, and then a direct spatial strategy over the course of  
513 training. By test days 4 and 5, wild type rats were using a search pattern that differed  
514 significantly by Chi square analysis from R237H rats ( $p < 0.05$  and  $p < 0.01$ , respectively) in that  
515 fewer wild type rats were using a random search strategy, and more were using a direct spatial

516 strategy. The same general pattern was found when all four daily trials were included in a Chi  
517 square analysis (Extended Data Fig. 8-1).

518

## 519 **Discussion**

520 Cognitive delays and deficits are frequent clinical features of Alexander disease, particularly in  
521 early onset cases, but relatively few publications provide detailed information about the  
522 cognitive phenotype. Most studies are single case reports, presenting evidence for cognitive  
523 decline using a variety of tests including unspecified IQ tests, Wechsler Intelligence scales for  
524 adults and children, and tests for dementia. More recent studies have provided additional  
525 information about cognitive function, including impaired visual and verbal memory, using  
526 different assessment tools. For example, memory problems were reported in 3 subjects with  
527 adult onset AxD, including impairments in short-term memory and tests of object recall (Anis et  
528 al., 2023). In another case study, 2 of 3 adult onset AxD patients showed impaired verbal and  
529 visual memory in the Montreal Cognitive Assessment (MoCA) test (Lichtenstein et al., 2017). In  
530 a study of four children with AxD, ages 5-15, verbal short-term memory, backwards verbal short-  
531 term memory and narrative microstructure were impaired, along with word recall (Zampini et al.,  
532 2023). Additional case studies of patients with infantile onset support the conclusion that  
533 cognitive impairments, and memory deficits in particular, are common features of AxD (Draghi  
534 et al., 2019; Kirsch et al., 2021), but a better understanding of the cognitive phenotype and its  
535 underlying mechanism is necessary for the development and testing of potential therapeutics to  
536 address this aspect of the disease.

537 Memory processes involve interactions among widespread regions of the brain,  
538 including prefrontal cortex, amygdala, striatum, and hippocampus among others (White and  
539 McDonald, 2002; Kesner, 2009), and astrocyte pathology throughout the CNS is likely to  
540 contribute to memory impairment found in AxD (Li et al., 2025). In this report, we sought to take



541 advantage of the R237H rat model of AxD to determine the impact of reactive and dysfunctional  
542 astrocytes on hippocampal neurons, memory, and learning. Transcriptomic analysis of  
543 hippocampal gene expression indicated early activation of stress related pathways in AxD  
544 model rats prior to onset of overt clinical phenotypes. Pathways related to immune processes  
545 were activated at 3 weeks of age and then intensified as disease progressed, similar to our  
546 previous transcriptomic studies in an early mouse model of AxD (Hagemann et al., 2005).  
547 Genes related to metabolism, particularly those involved in lipid and cholesterol biosynthesis,  
548 were down regulated at this early stage, and a subset of synaptic and neurodevelopmental  
549 transcripts were also decreased. The decline in synapse related gene expression became more  
550 pronounced with disease progression with multiple neuronal subtypes being implicated, and  
551 pathways involved in oxidative phosphorylation and mitochondrial function were also decreased,  
552 depicting a general profile of neurodegeneration. Given the essential role of astrocytes in  
553 maintaining CNS homeostasis and that AxD is a primary disorder of astrocytes, these results  
554 suggest that astrocyte dysfunction may also be a driving factor in other neurodegenerative  
555 diseases.

556 We recently reported that a subpopulation of astrocytes in AxD display a senescent  
557 phenotype, as demonstrated in multiple models, including the rat, and in patients with the  
558 disease (Wang et al., 2022). In addition, we have shown that gene expression profiles from our  
559 mouse models of AxD are highly congruent with a transcriptomic portrait of human Alzheimer's  
560 disease, second only to the Alzheimer's APP/PSEN1 mouse in comparisons with large-scale  
561 gene expression data from over 500 animal models (Gammie et al., 2024). These results further  
562 suggest that chronic gliosis and astrocyte dysfunction contribute to cognitive impairment in both  
563 Alzheimer's disease and AxD, and early reports described AxD as a developmental form of  
564 Alzheimer's based on the marked oxidative stress response (Castellani et al., 1999). Here we  
565 find overlap between these two conditions in both the stress response and in the loss of

566 markers for synaptic and mitochondrial function. Whether metabolic changes occur in neurons,  
567 astrocytes, or multiple cell types is not clear, but studies with induced pluripotent stem cell  
568 derived astrocytes from patients with AxD also demonstrate shifts in glycolysis and oxidative  
569 phosphorylation (Jones et al., 2018). Intermediate filaments have direct and indirect interactions  
570 with mitochondria (Schwarz and Leube, 2016), and GFAP mutations have been linked to  
571 lipoxidation and oxidative stress (Viedma-Poyatos et al., 2022). Mitochondrial dysfunction may  
572 also contribute to a cell-intrinsic innate immune response (Banoth and Cassel, 2018; Newman  
573 and Shadel, 2023), and future studies on the role of lipid metabolism and mitochondrial function  
574 will be important in understanding how astrocytes contribute to the neurodegenerative profile  
575 (Cali et al., 2024).

576 Immune-related responses are prominent at an early age in rodent models of AxD  
577 (Hagemann et al., 2005; Olabarria et al., 2015), and although neuroinflammation precedes  
578 severe cognitive deficits in neurodegenerative disorders of aging such as Alzheimer's disease,  
579 effects on mild cognitive impairment in early stages of disease are not clear (Heneka et al.,  
580 2015). Microglia play a pivotal role in recognizing amyloid  $\beta$  as a DAMP and triggering innate  
581 immune signaling, and although reactive astrocytes contribute to the inflammatory milieu,  
582 genetic risk factors such as TREM2 and CD33 variants implicate microglia as key players in  
583 Alzheimer's disease. In AxD, the primary insult is in astrocytes, but many of the same genes  
584 and pathways are activated in both diseases. Astrocyte specific transcription profiling in AxD  
585 model mice at postnatal day 14, an early stage in GFAP accumulation and aggregation, shows  
586 a similar elevation in innate immune related transcripts (Gammie et al., 2024), and our recent  
587 study analyzing the role of STAT3 in GFAP elevation and the astrocyte stress response further  
588 indicates that the immune response is initiated in astrocytes (Hagemann et al., 2023).  
589 Nevertheless, microglia are reactive and in close association with astrocytes in AxD (Olabarria  
590 et al., 2015; Hagemann et al., 2021), and innate immune pathways are likely activated in both

591 cell types. Future studies will include single cell analysis to follow the trajectory of astrocyte  
592 pathology within different subtypes and non-cell-autonomous effects on microglia, neurons, and  
593 oligodendrocytes over time (Srinivasan et al., 2016; Mathys et al., 2019; Habib et al., 2020;  
594 Liddel et al., 2020; Allen et al., 2022; Sadick et al., 2022; Mathys et al., 2024; O'Dea and  
595 Hasel, 2024).

596 The importance of the hippocampus for memory is well established (Scoville and Milner,  
597 1957; Squire and Zola-Morgan, 1991), but the specific contributions of hippocampal subregions  
598 (e.g., dentate gyrus, CA1, CA3) and adjacent structures (e.g., perirhinal, entorhinal cortex) to  
599 explicit aspects of memory are still not well understood (Hainmueller and Bartos, 2020). To  
600 assess whether reduced expression of synaptic markers reflect neuronal loss in R237H rats, we  
601 quantified granule cells in the dentate gyrus and pyramidal cells in CA1 and CA3 and found no  
602 change at 3 weeks but reduced numbers of granule cells at 8 weeks of age. We have previously  
603 shown that AxD model mice and rats exhibit deficits in adult neurogenesis, with virtually no  
604 detectable doublecortin expressing neurons (Hagemann et al., 2013; Hagemann et al., 2021),  
605 which may contribute to the differences in cell number observed in the dentate gyrus. Further  
606 analysis of synaptic proteins demonstrated a decrease in pre- and post-synaptic markers for  
607 both excitatory and inhibitory synapses, suggesting that neuronal deficits are not selective and  
608 supporting our transcriptomic analysis showing downregulation of several neurotransmitter  
609 signaling pathways including those for glutamatergic and GABAergic synapses. Importantly, we  
610 demonstrate that neuronal deficits translate into functional deficits, both physiologically with  
611 reduced hippocampal long-term potentiation and synaptic plasticity, and behaviorally with  
612 impaired performance in tests of learning and memory. These findings contrast with earlier work  
613 showing increased hippocampal long-term potentiation and plasticity in GFAP-null mice (McCall  
614 et al., 1996), and further demonstrate the toxic gain-of-function caused by GFAP mutation.

615           Given the many differences we observed in immune factors, metabolic pathways, and  
616 synaptic proteins, and their potential effects on neurodevelopment, synaptic plasticity, and  
617 cognitive functions, we cannot attribute a single cause for impaired LTP and cognitive deficits in  
618 the R237H rat (Li et al., 2025). Astrocytes are intricately associated with synapses and respond  
619 to many of the same neurotransmitters via G-protein coupled receptor activation and  
620 intracellular calcium mobilization (Durkee and Araque, 2019), and previous studies have shown  
621 that  $Ca^{2+}$  dependent astrocyte release of D-serine is necessary for NMDA receptor activation  
622 and LTP induction (Henneberger et al., 2010; Adamsky et al., 2018; Ahrens et al., 2024). A  
623 recent report further demonstrates activation of c-Fos and increased  $Ca^{2+}$  activity in  
624 hippocampal astrocytes associated with engram neurons during contextual fear conditioning,  
625 and astrocyte-specific knockout of c-Fos reduces  $Ca^{2+}$  activity, impairs learning, and diminishes  
626 hippocampal LTP (Williamson et al., 2025). Astrocytes in mouse models of AxD (Saito et al.,  
627 2018) and induced pluripotent stem cell derived astrocytes from patients with the disease  
628 (Jones et al., 2018) demonstrate aberrant  $Ca^{2+}$  waves, and the transcriptomic analysis reported  
629 here shows reduced expression of genes related to calcium signaling. The marked reduction in  
630 LTP in the R237H rat model provides an opportunity for future studies to determine the degree  
631 to which loss of normal astrocyte function contributes to reduced synaptic plasticity in AxD.

632           Several overlapping memory processes have been proposed for the dentate gyrus,  
633 including novelty detection (Hunsaker et al., 2008), recognition memory (Jiang et al., 2023),  
634 pattern separation (Gilbert et al., 2001), pattern completion (Nakashiba et al., 2012), binding of  
635 information to spatial contexts (Lee and Jung, 2017), and working memory (Sasaki et al., 2018).  
636 Given the crucial role of the hippocampus in the formation and recall of memories for objects,  
637 places, and events (Lisman et al., 2017), abnormalities in the dentate gyrus likely contribute to  
638 deficits in both novel object recognition and the Barnes maze, as observed in AxD model rats.  
639 Computational modeling suggests that dentate granule cells perform pattern-separation on

640 spatial representations arriving from the entorhinal cortex (Yassa and Stark, 2011; Kesner and  
641 Rolls, 2015), and recent optogenetic studies show that the perforant pathway, and more  
642 specifically projections from the medial entorhinal cortex layer II to the dentate, are an essential  
643 memory circuit for visually guided navigation tasks like the Barnes maze (Qin et al., 2018).  
644 Given the role of the perforant pathway in memory impairment in Alzheimer's disease (Hyman  
645 et al., 1987; Harris et al., 2010), astrocyte pathology and neuronal deficits in the entorhinal  
646 cortex may also be worth future investigation in AxD.

647         In this report, we show that in addition to motor and myelin deficits (Hagemann et al.,  
648 2021), the rat model of AxD demonstrates neuronal and cognitive impairment as clinically  
649 relevant phenotypes. Future studies can take advantage of the model to better understand  
650 astrocyte dysfunction in AxD and neurodegenerative disease more generally.

651 **References**

- 652 Adamsky A, Kol A, Kreisel T, Doron A, Ozeri-Engelhard N, Melcer T, Refaeli R, Horn H, Regev  
653 L, Groysman M, London M, Goshen I (2018) Astrocytic Activation Generates De Novo  
654 Neuronal Potentiation and Memory Enhancement. *Cell* 174:59-71.e14.
- 655 Ahrens MB, Khakh BS, Poskanzer KE (2024) Astrocyte Calcium Signaling. *Cold Spring Harb  
656 Perspect Biol* 16:a041353.
- 657 Alexander WS (1949) Progressive fibrinoid degeneration of fibrillary astrocytes associated with  
658 mental retardation in a hydrocephalic infant. *Brain* 72:373-381.
- 659 Allen DE, Donohue KC, Cadwell CR, Shin D, Keefe MG, Sohal VS, Nowakowski TJ (2022) Fate  
660 mapping of neural stem cell niches reveals distinct origins of human cortical astrocytes.  
661 *Science*:eabm5224.
- 662 Allen NJ, Eroglu C (2017) Cell Biology of Astrocyte-Synapse Interactions. *Neuron* 96:697-708.
- 663 Anis S, Fay-Karmon T, Lassman S, Shbat F, Lesman-Segev O, Mor N, Barel O, Dominissini D,  
664 Chorin O, Pras E, Greenbaum L, Hassin-Baer S (2023) Adult-onset Alexander disease  
665 among patients of Jewish Syrian descent. *Neurogenetics* 24:303-310.
- 666 Araque A, Parpura V, Sanzgiri RP, Haydon PG (1999) Tripartite synapses: glia, the  
667 unacknowledged partner. *Trends Neurosci* 22:208-215.
- 668 Banoth B, Cassel SL (2018) Mitochondria in innate immune signaling. *Transl Res* 202:52-68.
- 669 Barnes CA (1979) Memory deficits associated with senescence: a neurophysiological and  
670 behavioral study in the rat. *J Comp Physiol Psychol* 93:74-104.
- 671 Blanco-Suarez E, Caldwell AL, Allen NJ (2017) Role of astrocyte-synapse interactions in CNS  
672 disorders. *J Physiol* 595:1903-1916.

673 Borrett D, Becker LE (1985) Alexander's disease. A disease of astrocytes. *Brain* 108 ( Pt 2):367-  
674 385.

675 Boyd MM, Litscher SJ, Seitz LL, Messing A, Hagemann TL, Collier LS (2021) Pexidartinib  
676 treatment in Alexander disease model mice reduces macrophage numbers and  
677 increases glial fibrillary acidic protein levels, yet has minimal impact on other disease  
678 phenotypes. *J Neuroinflammation* 18:67.

679 Brenner M, Johnson AB, Boespflug-Tanguy O, Rodriguez D, Goldman JE, Messing A (2001)  
680 Mutations in GFAP, encoding glial fibrillary acidic protein, are associated with Alexander  
681 disease. *Nat Genet* 27:117-120.

682 Brown MW, Aggleton JP (2001) Recognition memory: what are the roles of the perirhinal cortex  
683 and hippocampus? *Nat Rev Neurosci* 2:51-61.

684 Cali C, Cantando I, Veloz Castillo MF, Gonzalez L, Bezzi P (2024) Metabolic Reprogramming of  
685 Astrocytes in Pathological Conditions: Implications for Neurodegenerative Diseases. *Int*  
686 *J Mol Sci* 25:8922.

687 Castellani RJ, Perry G, Brenner DS, Smith MA (1999) Alexander disease: Alzheimer disease of  
688 the developing brain? *Alzheimer Dis Assoc Disord* 13:232-235.

689 Dobin A, Davis CA, Schlesinger F, Drenkow J, Zaleski C, Jha S, Batut P, Chaisson M, Gingeras  
690 TR (2013) STAR: ultrafast universal RNA-seq aligner. *Bioinformatics* 29:15-21.

691 Draghi L, Salsano E, Farina L, Di Bella D, Fenu S, Pareyson D, Taroni F, Piacentini S (2019)  
692 Neuropsychological features of adult form of Alexander disease. *J Neurol Sci* 401:87-89.

693 Durkee CA, Araque A (2019) Diversity and Specificity of Astrocyte-neuron Communication.  
694 *Neuroscience* 396:73-78.

695 Ennaceur A, Delacour J (1988) A new one-trial test for neurobiological studies of memory in  
696 rats. 1: Behavioral data. Behav Brain Res 31:47-59.

697 Fedor M, Berman RF, Muizelaar JP, Lyeth BG (2010) Hippocampal  $\theta$  dysfunction after lateral  
698 fluid percussion injury. J Neurotrauma 27:1605-1615.

699 Gammie SC, Messing A, Hill MA, Kelm-Nelson CA, Hagemann TL (2024) Large-scale gene  
700 expression changes in APP/PSEN1 and GFAP mutation models exhibit high congruence  
701 with Alzheimer's disease. PLoS One 19:e0291995.

702 Gilbert PE, Kesner RP, Lee I (2001) Dissociating hippocampal subregions: double dissociation  
703 between dentate gyrus and CA1. Hippocampus 11:626-636.

704 Habib N, McCabe C, Medina S, Varshavsky M, Kitsberg D, Dvir-Szternfeld R, Green G, Dionne  
705 D, Nguyen L, Marshall JL, Chen F, Zhang F, Kaplan T, Regev A, Schwartz M (2020)  
706 Disease-associated astrocytes in Alzheimer's disease and aging. Nat Neurosci 23:701-  
707 706.

708 Hagemann TL (2022) Alexander disease: models, mechanisms, and medicine. Curr Opin  
709 Neurobiol 72:140-147.

710 Hagemann TL, Connor JX, Messing A (2006) Alexander disease-associated glial fibrillary acidic  
711 protein mutations in mice induce Rosenthal fiber formation and a white matter stress  
712 response. J Neurosci 26:11162-11173.

713 Hagemann TL, Paylor R, Messing A (2013) Deficits in adult neurogenesis, contextual fear  
714 conditioning, and spatial learning in a Gfap mutant mouse model of Alexander disease. J  
715 Neurosci 33:18698-18706.

716 Hagemann TL, Gaeta SA, Smith MA, Johnson DA, Johnson JA, Messing A (2005) Gene  
717 expression analysis in mice with elevated glial fibrillary acidic protein and Rosenthal



718 fibers reveals a stress response followed by glial activation and neuronal dysfunction.  
719 Hum Mol Genet 14:2443-2458.

720 Hagemann TL, Coyne S, Levin A, Wang L, Feany MB, Messing A (2023) STAT3 Drives GFAP  
721 Accumulation and Astrocyte Pathology in a Mouse Model of Alexander Disease. Cells  
722 12:978.

723 Hagemann TL, Powers B, Lin NH, Mohamed AF, Dague KL, Hannah SC, Bachmann G, Mazur  
724 C, Rigo F, Olsen AL, Feany MB, Perng MD, Berman RF, Messing A (2021) Antisense  
725 therapy in a rat model of Alexander disease reverses GFAP pathology, white matter  
726 deficits, and motor impairment. Sci Transl Med 13:eabg4711.

727 Hainmueller T, Bartos M (2020) Dentate gyrus circuits for encoding, retrieval and discrimination  
728 of episodic memories. Nat Rev Neurosci 21:153-168.

729 Harris JA, Devidze N, Verret L, Ho K, Halabisky B, Thwin MT, Kim D, Hamto P, Lo I, Yu GQ,  
730 Palop JJ, Masliah E, Mucke L (2010) Transsynaptic progression of amyloid- $\beta$ -induced  
731 neuronal dysfunction within the entorhinal-hippocampal network. Neuron 68:428-441.

732 Heneka MT et al. (2015) Neuroinflammation in Alzheimer's disease. Lancet Neurol 14:388-405.

733 Henneberger C, Papouin T, Oliet SH, Rusakov DA (2010) Long-term potentiation depends on  
734 release of D-serine from astrocytes. Nature 463:232-236.

735 Hunsaker MR, Rosenberg JS, Kesner RP (2008) The role of the dentate gyrus, CA3a,b, and  
736 CA3c for detecting spatial and environmental novelty. Hippocampus 18:1064-1073.

737 Hyman BT, Kromer LJ, Van Hoesen GW (1987) Reinnervation of the hippocampal perforant  
738 pathway zone in Alzheimer's disease. Ann Neurol 21:259-267.

739 Jiang H, Lei R, Ding SW, Zhu S (2014) Skewer: a fast and accurate adapter trimmer for next-  
740 generation sequencing paired-end reads. BMC Bioinformatics 15:182.

741 Jiang YK, Dong FY, Dong YB, Zhu XY, Pan LH, Hu LB, Xu L, Xu XF, Xu LM, Zhang XQ (2023)  
742 Lateral septal nucleus, dorsal part, and dentate gyrus are necessary for spatial and  
743 object recognition memory, respectively, in mice. *Front Behav Neurosci* 17:1139737.

744 Jones JR, Kong L, Hanna MGt, Hoffman B, Krencik R, Bradley R, Hagemann T, Choi J, Doers  
745 M, Dubovis M, Sherafat MA, Bhattacharyya A, Kendzioriski C, Audhya A, Messing A,  
746 Zhang SC (2018) Mutations in GFAP Disrupt the Distribution and Function of Organelles  
747 in Human Astrocytes. *Cell Rep* 25:947-958 e944.

748 Kanehisa M, Goto S (2000) KEGG: kyoto encyclopedia of genes and genomes. *Nucleic Acids*  
749 *Res* 28:27-30.

750 Kesner RP (2009) Tapestry of memory. *Behav Neurosci* 123:1-13.

751 Kesner RP, Rolls ET (2015) A computational theory of hippocampal function, and tests of the  
752 theory: new developments. *Neurosci Biobehav Rev* 48:92-147.

753 Kinnavane L, Albasser MM, Aggleton JP (2015) Advances in the behavioural testing and  
754 network imaging of rodent recognition memory. *Behav Brain Res* 285:67-78.

755 Kirsch AC, McCall DM, Lange H, Renaud D, Brown T, Zaccariello MJ (2021)  
756 Neuropsychological Functioning in Alexander Disease: A Case Series. *Child Neurol*  
757 *Open* 8:2329048X211048614.

758 Lee JW, Jung MW (2017) Separation or binding? Role of the dentate gyrus in hippocampal  
759 mnemonic processing. *Neurosci Biobehav Rev* 75:183-194.

760 Li B, Dewey CN (2011) RSEM: accurate transcript quantification from RNA-Seq data with or  
761 without a reference genome. *BMC Bioinformatics* 12:323.

762 Li S, Chen Y, Chen G (2025) Cognitive disorders: Potential astrocyte-based mechanism. *Brain*  
763 *Res Bull* 220:111181.

764 Li T, Chen ZJ (2018) The cGAS-cGAMP-STING pathway connects DNA damage to  
765 inflammation, senescence, and cancer. *J Exp Med* 215:1287-1299.

766 Lichtenstein ML, Dwosh E, Roy Chowdhury A, Farrer MJ, McKenzie MB, Guella I, Evans DM,  
767 Nygaard HB, Shewchuk JR, Hayden S, Barton JJS, Feldman HH (2017)  
768 Neurobehavioral characterization of adult-onset Alexander disease: A family study.  
769 *Neurol Clin Pract* 7:425-429.

770 Liddelow SA, Marsh SE, Stevens B (2020) Microglia and Astrocytes in Disease: Dynamic Duo  
771 or Partners in Crime? *Trends Immunol* 41:820-835.

772 Lisman J, Buzsáki G, Eichenbaum H, Nadel L, Ranganath C, Redish AD (2017) Viewpoints:  
773 how the hippocampus contributes to memory, navigation and cognition. *Nat Neurosci*  
774 20:1434-1447.

775 Mathys H, Davila-Velderrain J, Peng Z, Gao F, Mohammadi S, Young JZ, Menon M, He L,  
776 Abdurrob F, Jiang X, Martorell AJ, Ransohoff RM, Hafler BP, Bennett DA, Kellis M, Tsai  
777 LH (2019) Single-cell transcriptomic analysis of Alzheimer's disease. *Nature* 570:332-  
778 337.

779 Mathys H, Boix CA, Akay LA, Xia Z, Davila-Velderrain J, Ng AP, Jiang X, Abdelhady G, Galani  
780 K, Mantero J, Band N, James BT, Babu S, Galiana-Melendez F, Louderback K,  
781 Prokopenko D, Tanzi RE, Bennett DA, Tsai L-H, Kellis M (2024) Single-cell multiregion  
782 dissection of Alzheimer's disease. *Nature* 632:858-868.

783 McCall MA, Gregg RG, Behringer RR, Brenner M, Delaney CL, Galbreath EJ, Zhang CL,  
784 Pearce RA, Chiu SY, Messing A (1996) Targeted deletion in astrocyte intermediate  
785 filament (Gfap) alters neuronal physiology. *Proc Natl Acad Sci U S A* 93:6361-6366.

786 Messing A (2019) Refining the concept of GFAP toxicity in Alexander disease. *J Neurodev*  
787 *Disord* 11:27.

788 Messing A, Brenner M, Feany MB, Nedergaard M, Goldman JE (2012) Alexander disease. *J*  
789 *Neurosci* 32:5017-5023.

790 Morris R (1984) Developments of a water-maze procedure for studying spatial learning in the  
791 rat. *J Neurosci Methods* 11:47-60.

792 Nakashiba T, Cushman JD, Pelkey KA, Renaudineau S, Buhl DL, McHugh TJ, Rodriguez  
793 Barrera V, Chittajallu R, Iwamoto KS, McBain CJ, Fanselow MS, Tonegawa S (2012)  
794 Young dentate granule cells mediate pattern separation, whereas old granule cells  
795 facilitate pattern completion. *Cell* 149:188-201.

796 Newman LE, Shadel GS (2023) Mitochondrial DNA Release in Innate Immune Signaling. *Annu*  
797 *Rev Biochem* 92:299-332.

798 O'Dea MR, Hasel P (2024) Are we there yet? Exploring astrocyte heterogeneity one cell at a  
799 time. *Glia* DOI: 10.1002/glia.24621.

800 Olabarria M, Putilina M, Riemer EC, Goldman JE (2015) Astrocyte pathology in Alexander  
801 disease causes a marked inflammatory environment. *Acta Neuropathol* 130:469-486.

802 Pitts MW (2018) Barnes Maze Procedure for Spatial Learning and Memory in Mice. *Bio Protoc*  
803 8.

804 Prust M et al. (2011) GFAP mutations, age at onset, and clinical subtypes in Alexander disease.  
805 *Neurology* 77:1287-1294.

806 Qin H, Fu L, Hu B, Liao X, Lu J, He W, Liang S, Zhang K, Li R, Yao J, Yan J, Chen H, Jia H,  
807 Zott B, Konnerth A, Chen X (2018) A Visual-Cue-Dependent Memory Circuit for Place  
808 Navigation. *Neuron* 99:47-55.

809 Raudvere U, Kolberg L, Kuzmin I, Arak T, Adler P, Peterson H, Vilo J (2019) g:Profiler: a web  
810 server for functional enrichment analysis and conversions of gene lists (2019 update).  
811 Nucleic Acids Res 47:W191-w198.

812 Robinson MD, McCarthy DJ, Smyth GK (2010) edgeR: a Bioconductor package for differential  
813 expression analysis of digital gene expression data. Bioinformatics 26:139-140.

814 Sadick JS, O'Dea MR, Hasel P, Dykstra T, Faustin A, Liddel SA (2022) Astrocytes and  
815 oligodendrocytes undergo subtype-specific transcriptional changes in Alzheimer's  
816 disease. Neuron 110:1788-1805 e1710.

817 Saito K, Shigetomi E, Yasuda R, Sato R, Nakano M, Tashiro K, Tanaka KF, Ikenaka K,  
818 Mikoshiba K, Mizuta I, Yoshida T, Nakagawa M, Mizuno T, Koizumi S (2018) Aberrant  
819 astrocyte Ca(2+) signals "AxCa signals" exacerbate pathological alterations in an  
820 Alexander disease model. Glia 66:1053-1067.

821 Sasaki T, Piatti VC, Hwaun E, Ahmadi S, Lisman JE, Leutgeb S, Leutgeb JK (2018) Dentate  
822 network activity is necessary for spatial working memory by supporting CA3 sharp-wave  
823 ripple generation and prospective firing of CA3 neurons. Nat Neurosci 21:258-269.

824 Schwarz N, Leube RE (2016) Intermediate Filaments as Organizers of Cellular Space: How  
825 They Affect Mitochondrial Structure and Function. Cells 5:30.

826 Scoville WB, Milner B (1957) Loss of recent memory after bilateral hippocampal lesions. J  
827 Neurol Neurosurg Psychiatry 20:11-21.

828 Sirenko O, Böcker U, Morris JS, Haskill JS, Watson JM (2002) IL-1 beta transcript stability in  
829 monocytes is linked to cytoskeletal reorganization and the availability of mRNA  
830 degradation factors. Immunol Cell Biol 80:328-339.

831 Sivakumaran MH, Mackenzie AK, Callan IR, Ainge JA, O'Connor AR (2018) The Discrimination  
832 Ratio derived from Novel Object Recognition tasks as a Measure of Recognition Memory  
833 Sensitivity, not Bias. *Sci Rep* 8:11579.

834 Sosunov A, Olabarria M, Goldman JE (2018) Alexander disease: an astrocytopathy that  
835 produces a leukodystrophy. *Brain Pathol* 28:388-398.

836 Squire LR, Zola-Morgan S (1991) The medial temporal lobe memory system. *Science*  
837 253:1380-1386.

838 Srinivasan K, Friedman BA, Larson JL, Lauffer BE, Goldstein LD, Appling LL, Borneo J, Poon  
839 C, Ho T, Cai F, Steiner P, van der Brug MP, Modrusan Z, Kaminker JS, Hansen DV  
840 (2016) Untangling the brain's neuroinflammatory and neurodegenerative transcriptional  
841 responses. *Nat Commun* 7:11295.

842 van der Knaap MS, Naidu S, Breiter SN, Blaser S, Stroink H, Springer S, Begeer JC, van Coster  
843 R, Barth PG, Thomas NH, Valk J, Powers JM (2001) Alexander disease: diagnosis with  
844 MR imaging. *AJNR Am J Neuroradiol* 22:541-552.

845 Viedma-Poyatos Á, González-Jiménez P, Pajares MA, Pérez-Sala D (2022) Alexander disease  
846 GFAP R239C mutant shows increased susceptibility to lipoxidation and elicits  
847 mitochondrial dysfunction and oxidative stress. *Redox Biol* 55:102415.

848 Wang L, Bukhari H, Kong L, Hagemann TL, Zhang SC, Messing A, Feany MB (2022) Anastasis  
849 Drives Senescence and Non-Cell Autonomous Neurodegeneration in the Astrogliaopathy  
850 Alexander Disease. *J Neurosci* 42:2584-2597.

851 White NM, McDonald RJ (2002) Multiple parallel memory systems in the brain of the rat.  
852 *Neurobiol Learn Mem* 77:125-184.

853 Williamson MR, Kwon W, Woo J, Ko Y, Maleki E, Yu K, Murali S, Sardar D, Deneen B (2025)  
854 Learning-associated astrocyte ensembles regulate memory recall. *Nature* 637:478-486.

855 Wilson DM, 3rd, Cookson MR, Van Den Bosch L, Zetterberg H, Holtzman DM, Dewachter I  
856 (2023) Hallmarks of neurodegenerative diseases. *Cell* 186:693-714.

857 Winters BD, Saksida LM, Bussey TJ (2008) Object recognition memory: neurobiological  
858 mechanisms of encoding, consolidation and retrieval. *Neurosci Biobehav Rev* 32:1055-  
859 1070.

860 Yassa MA, Stark CE (2011) Pattern separation in the hippocampus. *Trends Neurosci* 34:515-  
861 525.

862 Zampini L, Draghi L, Zanchi P (2023) Developmental Profiles in Children and Young Adults with  
863 Alexander Disease. *Dev Neurorehabil* 26:253-261.

864 Zhao W, Wang L, Zhang M, Wang P, Qi J, Zhang L, Gao C (2012) Nuclear to cytoplasmic  
865 translocation of heterogeneous nuclear ribonucleoprotein U enhances TLR-induced  
866 proinflammatory cytokine production by stabilizing mRNAs in macrophages. *J Immunol*  
867 188:3179-3187.

868

869 **Figure legends**

870 **Figure 1.** Neurodegenerative profile of hippocampal transcripts in R237H rat model of AxD. **(A)**  
871 Volcano plot showing fold change ( $\log_2FC$ ) values versus the false discovery rate ( $\log_{10}FDR$ ) for  
872 differentially expressed genes (DEG) in 8-week-old male R237H rats compared to wild type  
873 ( $FDR < 0.01$ .) Genes related to the immune system process (GO:0002376) are highlighted in  
874 red, and those related to synapses (GO:0045202) are in blue. **(B)** Venn diagrams showing  
875 overlap in the number of DEG (increased and decreased) at P21 and P56. **(C)** Enrichment  
876 analysis for gene ontology (GO) terms and KEGG pathways for DEG ( $FDR < 0.01$ ) in male rats  
877 at 8 weeks of age ( $N=4$ ). For pathways with a  $-\log_{10}$  adjusted P value greater than 20, values  
878 are indicated within the graph. **(D)** Venn diagrams showing overlap in the number of DEG  
879 related to different GO terms: Immune system process (GO:0002376), Innate immune response  
880 (GO:0045087), Synapse (GO:0045202), and Mitochondrion (GO:0005739) at P21 and P56. **(E)**  
881 Heat maps for DEG between wild type (WT) versus R237H (RH) rats within male (M) or female  
882 (F) groups, at P21 or P56 matched to different GO term gene lists as indicated. Average TPM  
883 (transcripts per million) values were transformed to the color-coded minimum and maximum  
884 scale for each gene and K-means clustering used to highlight different patterns in  
885 developmental expression versus genotype related changes. For each group,  $N=4$ , except for  
886 WT females at P21,  $N=3$ ; and R237H females at P21,  $N=5$ . Extended Data Files 1-1, 1-2, 1-3,  
887 and 1-4 support this figure.

888

889 **Figure 2.** Neuroinflammatory response to GFAP mutation in AxD model rats. **(A)** Cytokines and  
890 chemokines were quantified by ELISA in adult R237H rats and WT littermate controls.  
891 Interleukins,  $IFN\gamma$ ,  $TNF\alpha$ , and CXCL1 were analyzed at 8 weeks, and the remaining chemokines  
892 were analyzed at 12 weeks of age. Data were analyzed with a 2-tailed unpaired  $t$ -test with  
893 Welch's correction,  $*p < 0.05$ ,  $**P < 0.01$ ,  $****p < 0.0001$ ,  $N = 5$  males and 5 females for each



894 group. Error bars are standard deviation. (B) Comparison of R237H versus WT fold change for  
895 transcript and protein expression for the same cytokines and chemokines shown in A (nd  
896 indicates transcript not detected).

897

898 **Figure 3.** Regional differences in hippocampal neuron numbers in R237H rats compared to wild  
899 type. Stereological counting of hippocampal neurons labeled with NeuN at P21 (A) and P56 (B).  
900 NeuN labeled nuclei were counted in the dentate gyrus granule cell layer (DG) and CA1 and  
901 CA3 pyramidal cell layers throughout the dorsal hippocampus (anterior boundary to posterior  
902 commissure). Data were analyzed by 2-way ANOVA and Sidak's multiple comparisons test (\*\*p  
903 = 0.0073, N = 6 per group consisting of 3 males and 3 females). There was no significant effect  
904 of sex when sex was included as a variable in a 3-way ANOVA.

905

906 **Figure 4.** Changes in synaptic protein expression in R237H rats. (A-B) Western analysis of pre-  
907 and post-synaptic proteins SV2A and PSD95 respectively in hippocampus. Representative  
908 images are shown for immunoblots and corresponding protein stain from the same region of the  
909 gel with molecular weight marker positions indicated on the right. Values for each protein are  
910 normalized to total protein and expressed as a fraction of the wild type group. (C-D) Western  
911 analysis of excitatory pre- and post-synaptic markers VGluT1 and GluA1 (E-F) and inhibitory  
912 markers VGAT and gephyrin. Data were analyzed with a 2-tailed unpaired *t*-test, \*p < 0.05, \*\*P  
913 < 0.01, \*\*\*\*p < 0.0001, N = 5 males and 5 females at 8 weeks of age for each group.

914

915 **Figure 5.** Changes in mitochondrial proteins in R237H rats. (A-B) Western analysis of subunits  
916 of the oxidative phosphorylation complexes I through V in rat hippocampus. (A) Representative  
917 images are shown for immunoblots and corresponding protein stain from the same region of the

918 gel with molecular weight marker positions indicated on the right. **(B)** Values for each subunit  
919 are normalized to total protein and expressed as a fraction of the wild type group. Data were  
920 analyzed with a 2-tailed unpaired *t*-test, \**p* < 0.05, \*\**P* < 0.01, \*\*\*\**p* < 0.0001, N = 3 males and 3  
921 females at 8 weeks of age for each group.

922

923 **Figure 6.** Deficits in hippocampal long-term potentiation in R237H rats. **(A)** Mean fEPSP slope  
924 for wild type (WT) animals before and after a theta-burst stimulation (TBS) paradigm with three  
925 trains of 10 bursts (4x100Hz). **(B)** Comparison of potentiation, defined as the average mean  
926 fEPSP slope during the last 10 minutes compared to baseline. Data were analyzed with a 2-  
927 tailed unpaired *t*-test, \*\*\**p* = 0.0008, N = 5 WT (2 male, 3 female), and 6 R237H (3 male, 3  
928 female) rats. Error bars = standard deviation.

929

930 **Figure 7.** Impaired novel object recognition (NOR) performance in R237H rats compared to wild  
931 type. **(A)** Time (seconds) exploring novel and familiar objects for wild type (WT) and R237H  
932 rats in the NOR test. Both novelty and genotype were significant sources of variation (novelty =  
933 9.5% of variation, *p* = 0.0033; genotype = 12.4% of variation, *p* = 0.0001; 2-way repeated  
934 measures ANOVA with uncorrected Fisher's LSD post-tests, *p* = 0.0104). **(B)** Discrimination  
935 index (DI) as a measure of NOR performance for WT and R237H rats. A DI significantly greater  
936 than 0.5 (chance) indicates a preference for exploration of the novel object, whereas a DI that is  
937 not significantly different from 0.5 indicates impairment in recognition memory (one sample *t*-  
938 test, \*\*\**p* = 0.0002). N = 24 WT (12 male, 12 female) and 24 R237H (12 male, 12 female) rats at  
939 16 weeks of age for A and B.

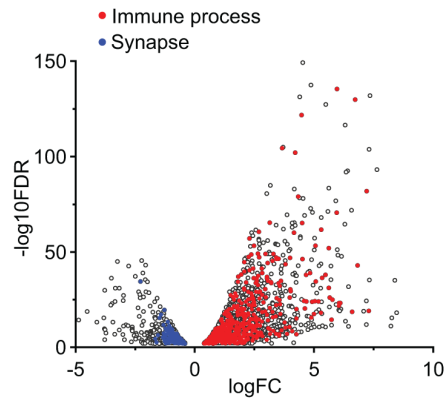
940

941 **Figure 8.** Barnes maze performance for wild type and R237H rats. **(A)** Latency to escape during  
942 the first trials over 5 consecutive days of training, ( $p = 0.018$  for effect of genotype, mixed-  
943 effects model;  $**p < 0.01$ , Sidak's post-test, error bars = SEM). **(B)** Search strategy patterns  
944 (random, serial, direct; see Methods section) used by rats to learn the location of the escape  
945 hole in the Barnes maze. The first trials for each of the 5 training days are shown for  
946 comparison between wild type (WT) and R237H rats (Chi Square;  $*p < 0.05$  and  $**p < 0.01$ ).  $N =$   
947 30 WT (14 male, 16 female), 24 R237H (11 male, 13 female), at 16 weeks of age for A and B.  
948 Average latency to escape and search strategies for all 4 trials are shown in Extended Data Fig.  
949 8-1.

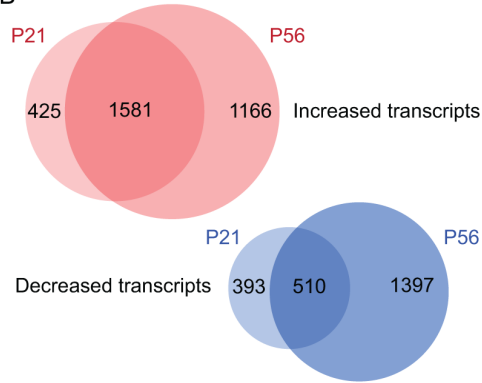
950

951

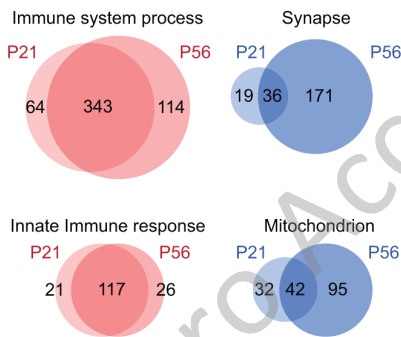
**A** Differentially expressed genes (FDR < 1%)



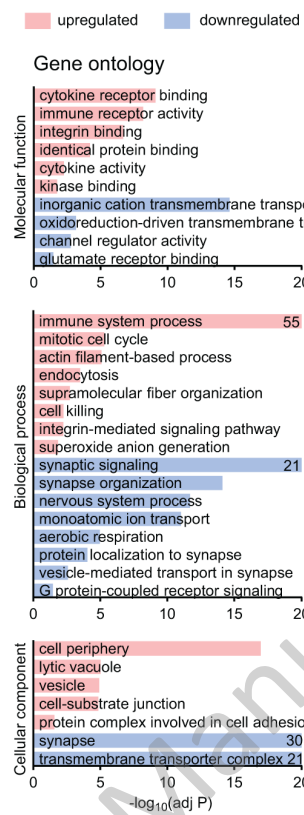
**B**



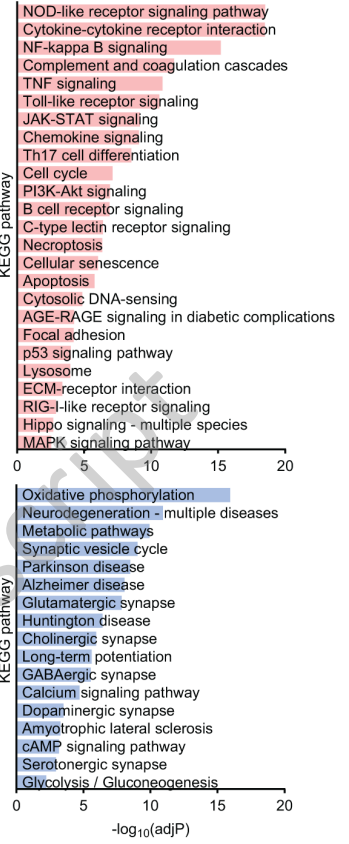
**D**



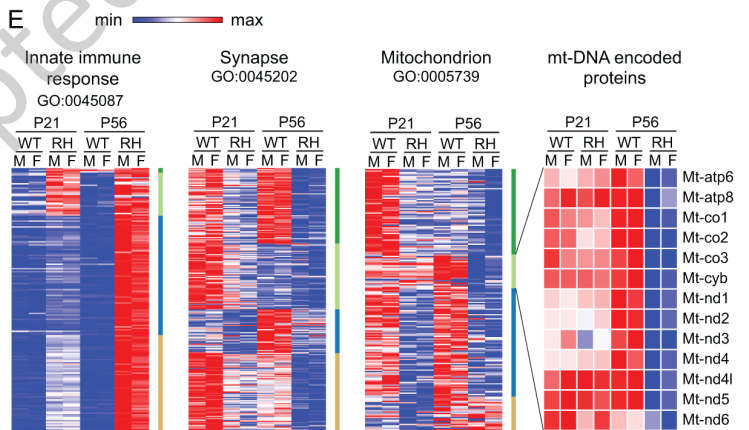
**C**

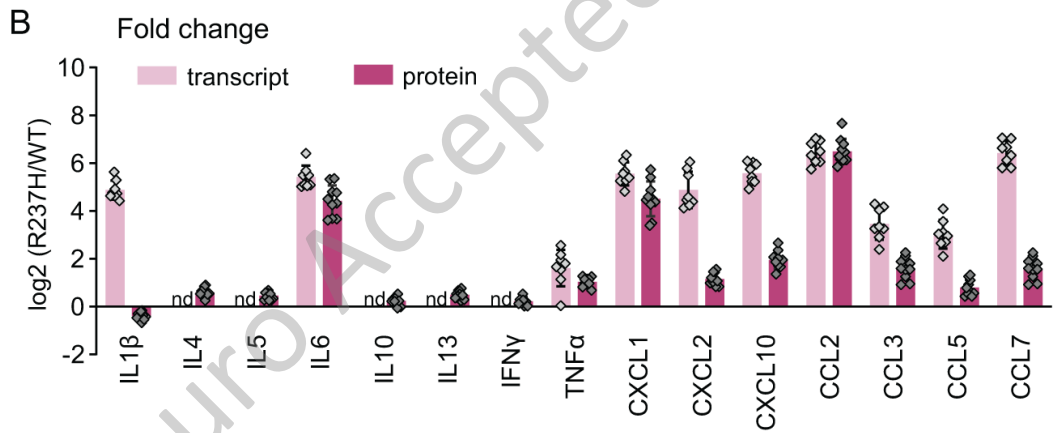
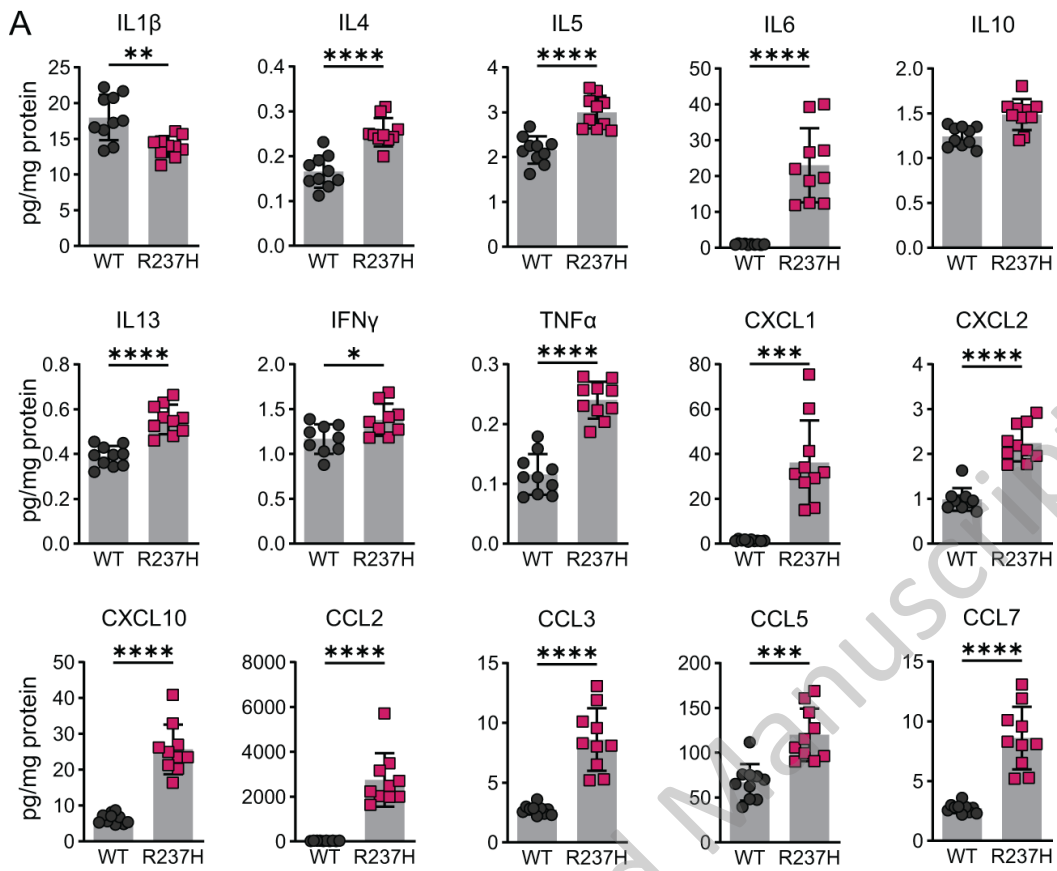


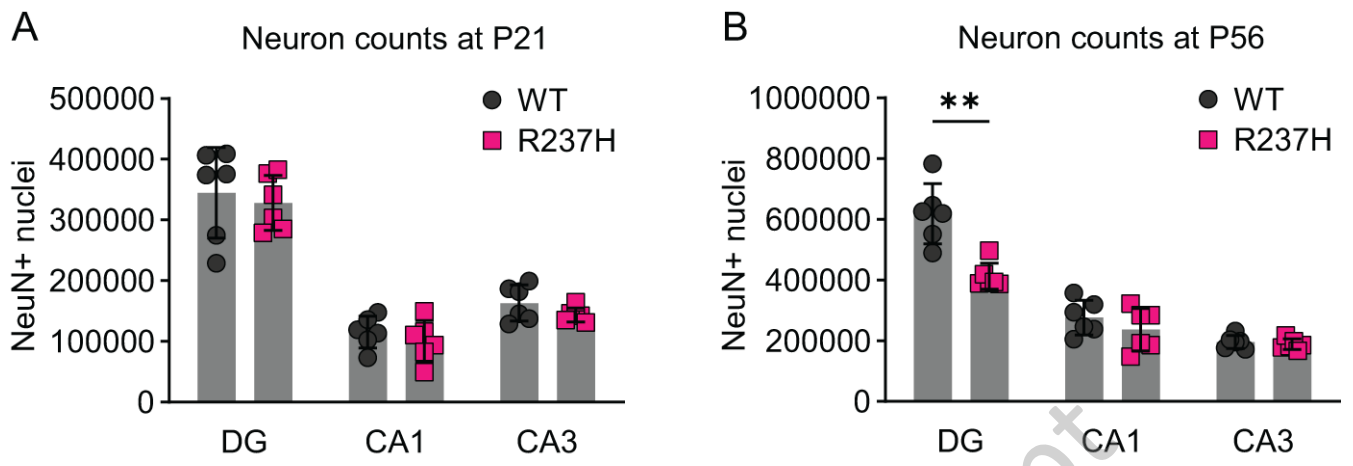
**Pathway enrichment**



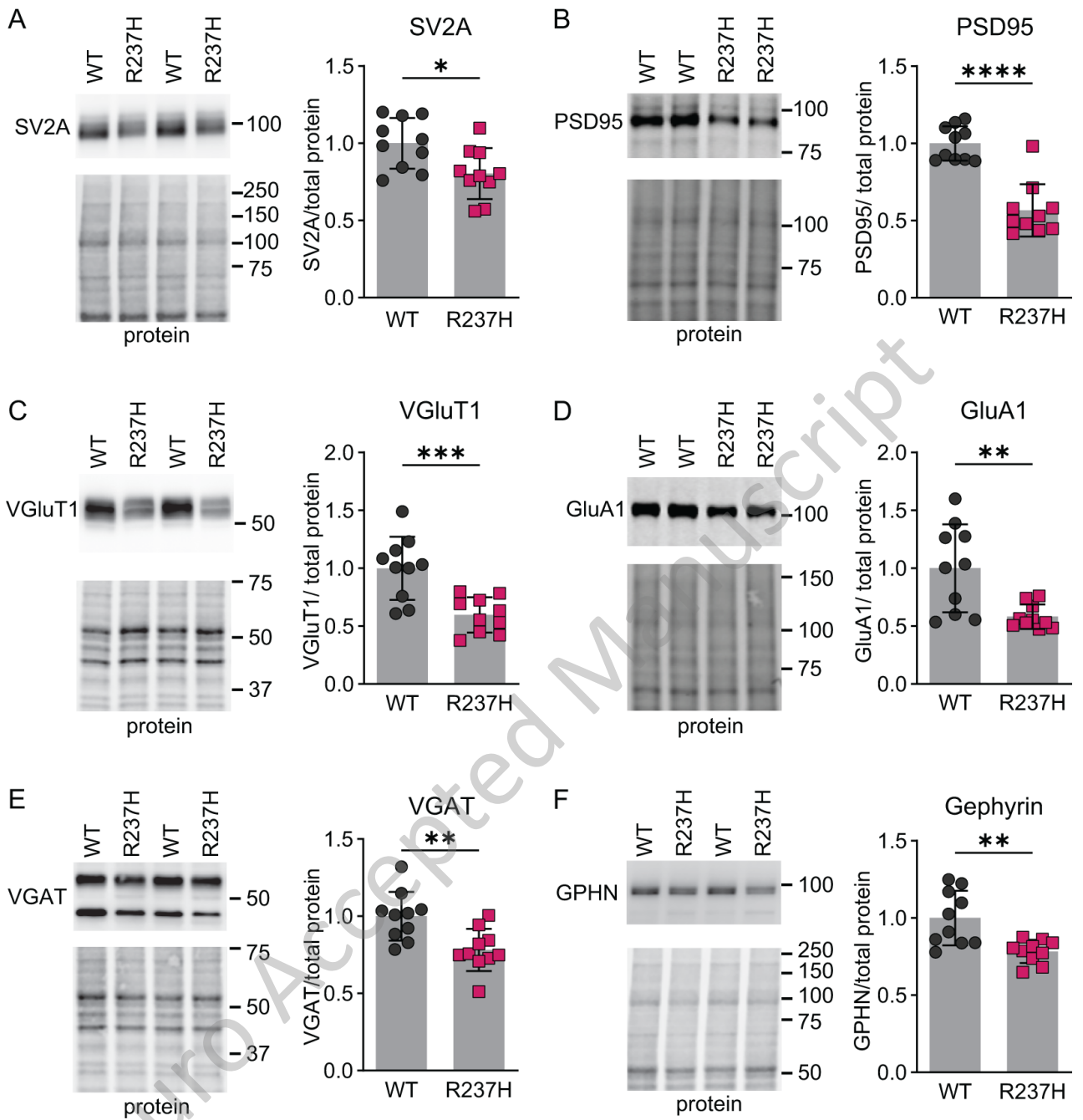
**E**

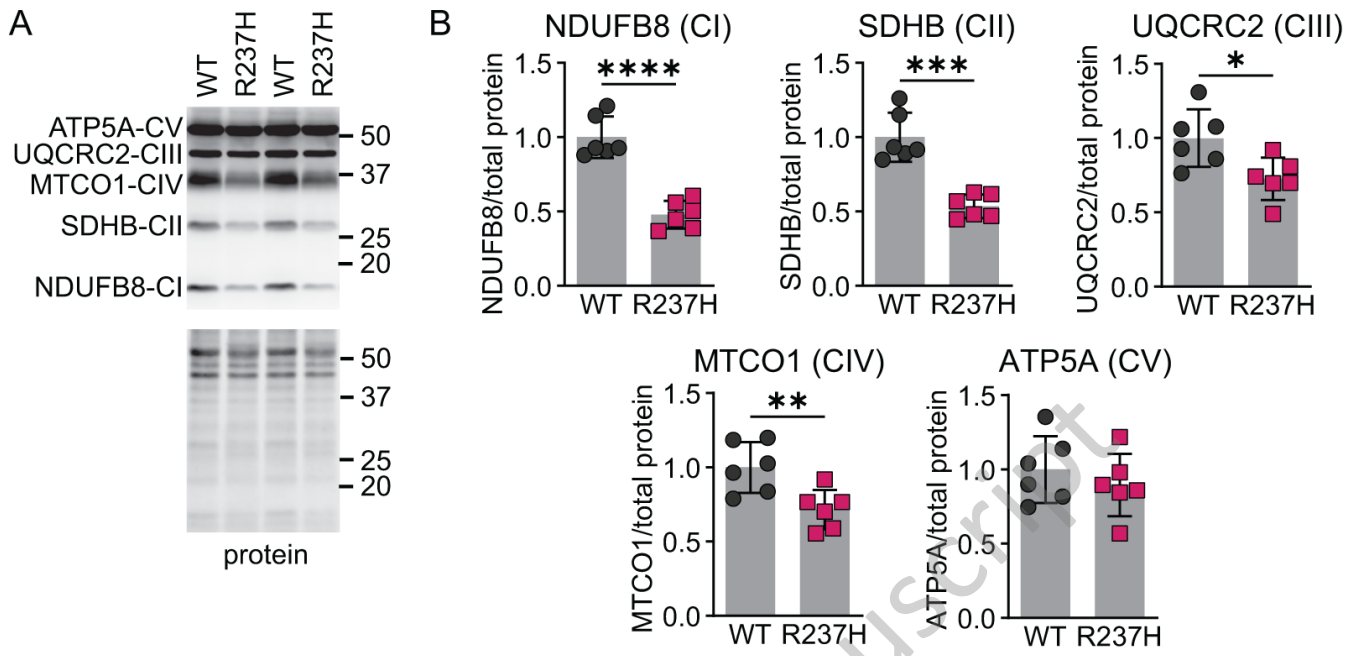






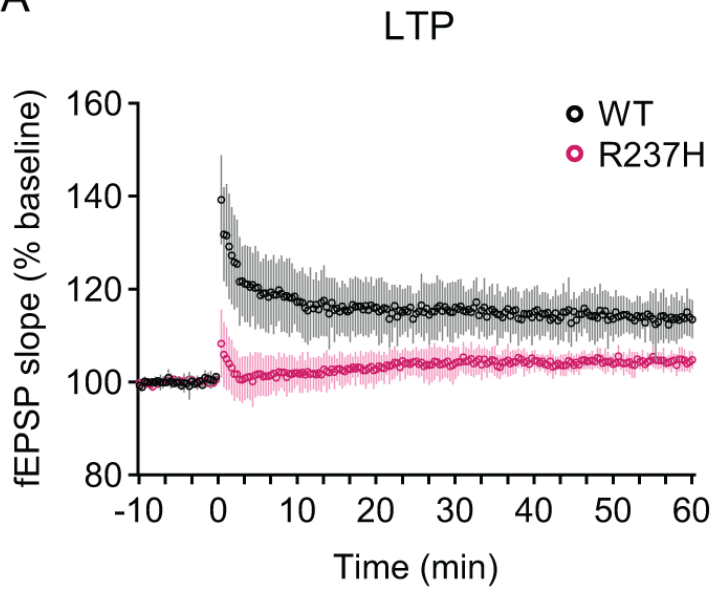
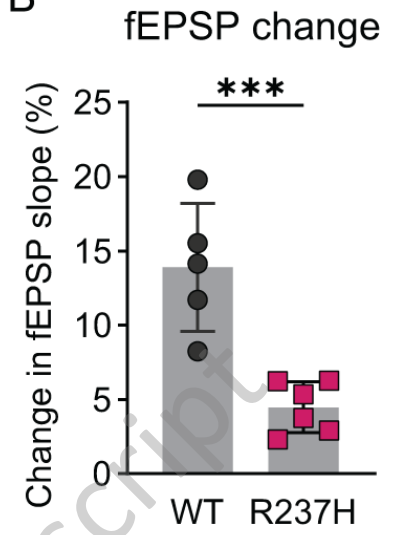
eNeuro Accepted Manuscript



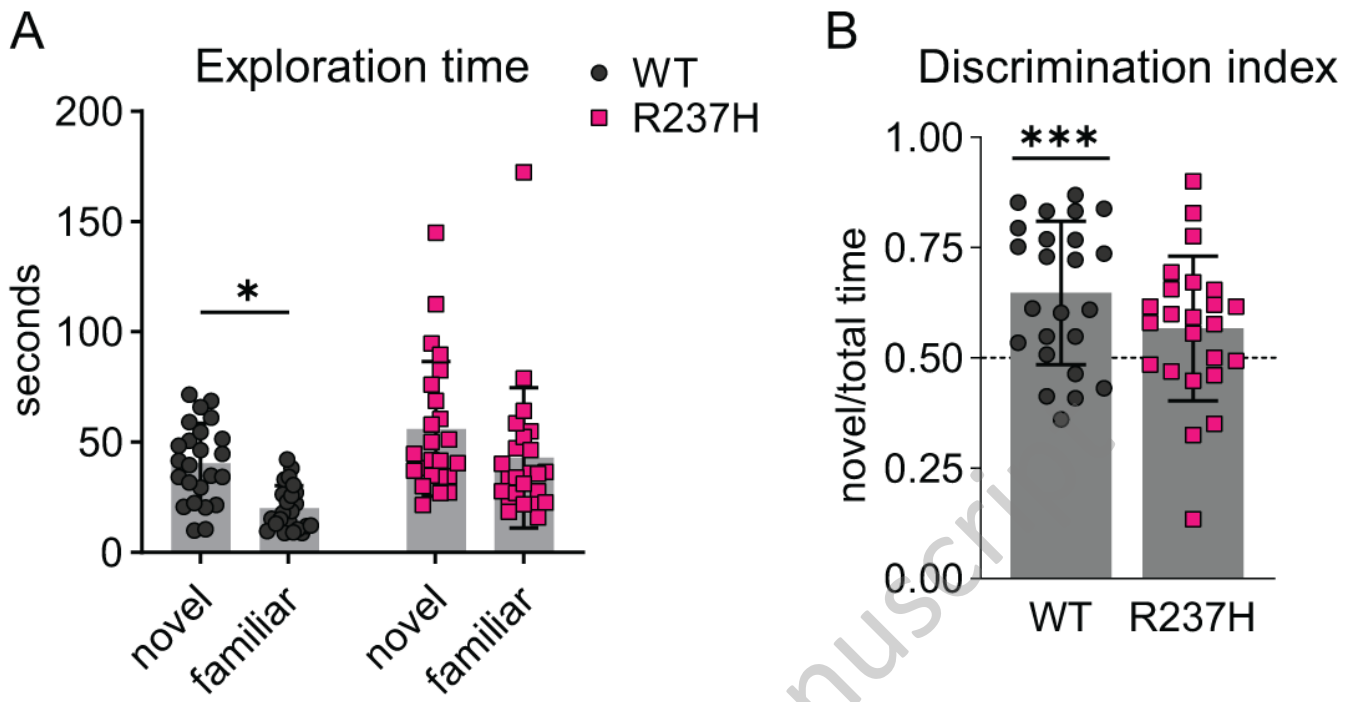


eNeuro Accepted Manuscript

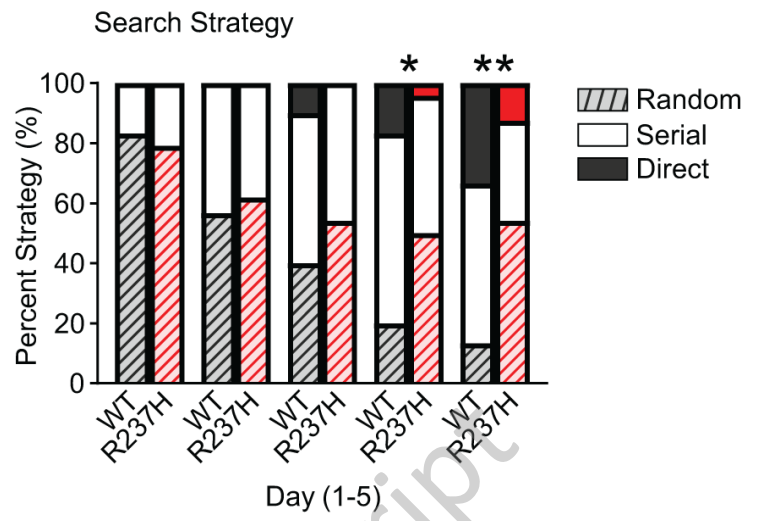
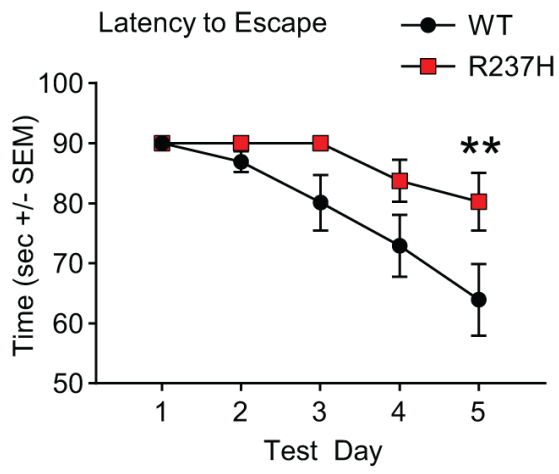


**A****B**

eNeuro Accepted Manuscript



eNeuro Accepted Manuscript



eNeuro Accepted Manuscript